



Well-Constrained Mineralization Ages by Integrated $^{40}\text{Ar}/^{39}\text{Ar}$ and U-Pb Dating Techniques for the Xitian W-Sn Polymetallic Deposit, South China[†]

Xiu-Juan Bai,^{1,2} Man Liu,³ Rong-Guo Hu,⁴ Yuan Fang,⁵ Xiao Liu,⁶ Bin Tang,⁶ and Hua-Ning Qiu^{1,2,†}

¹*Key Laboratory of Tectonics and Petroleum Resources (China University of Geosciences), Ministry of Education, Wuhan 430074, China*

²*School of Earth Resources, China University of Geosciences, Wuhan 430074, China*

³*No. 940 Branch of Nonferrous Metals Geological Bureau of Guangdong Province, Qingyuan 511520, China*

⁴*College of Earth Sciences, Guilin University of Technology, Guilin 541004, China*

⁵*State Key Laboratory of Isotope Geochronology and Geochemistry, Guangzhou Institute of Geochemistry, Chinese Academy of Sciences, Guangzhou 510640, China*

⁶*Institute of Nuclear Physics and Chemistry, China Academy of Engineering Physics, Mianyang 621900, China*

Abstract

Mineralization ages of many mineral deposit types (such as orogenic Au, stratabound Cu, and Mississippi Valley-type Pb-Zn deposits) are still difficult to date by the traditional isotopic chronometry because of the lack of suitable minerals. We have made efforts to establish a widely suitable dating technique to determine ore formation ages using a high-precision $^{40}\text{Ar}/^{39}\text{Ar}$ method on ubiquitously present fluid inclusions in quartz, sphalerite, and other nonpotassium minerals from hydrothermal deposits. The Xitian W-Sn polymetallic deposit in central South China contains several minerals suitable for isotopic dating for interchronometer comparison. $^{40}\text{Ar}/^{39}\text{Ar}$ laser step heating of 16 micas from ore veins, greisen, and metallogenetic granites yields flat age spectra and thus well-defined ore formation ages ranging from 152.4 ± 1.5 (2σ) to 148.1 ± 1.4 Ma with an average of 150.2 ± 0.6 Ma. $^{40}\text{Ar}/^{39}\text{Ar}$ progressive crushing of nine quartz samples produces well-defined isochron lines for their primary fluid inclusions corresponding to isochron ages of 153.7 – 149.9 Ma with an average of 151.6 ± 0.6 Ma. Cassiterites from three hand specimens have weighted mean $^{206}\text{Pb}/^{238}\text{U}$ ages of 151.5 ± 1.7 (2σ), 149.7 ± 2.1 , and 151.7 ± 2.1 Ma. All these new geochronological dates and previous molybdenite Re-Os ages yield well-constrained mineralization ages of 153 – 148 Ma for the Xitian W-Sn polymetallic deposit, which also confirms conclusively that the quartz $^{40}\text{Ar}/^{39}\text{Ar}$ progressive crushing technique is a feasible, valid dating technique. Furthermore, significant age information on the secondary fluid inclusions is potentially obtained simultaneously by this technique. We expect that this novel dating technique will be widely applied to determine the geologic fluids trapped in minerals during hydrothermal mineralization, hydrocarbon accumulation, metamorphism, tectonic activities, and other geologic processes.

Introduction

High-precision mineralization ages are very important to improve our understanding of ore-forming processes; however, it is still difficult to date many mineral deposit types (e.g., orogenic Au, stratabound Cu, and Mississippi Valley-type Pb-Zn deposits) by traditional isotopic chronometers because of the lack of suitable minerals. In order to establish a widely applicable approach of dating mineralization, we have endeavored to investigate the possibility of dating K-bearing fluid inclusions by $^{40}\text{Ar}/^{39}\text{Ar}$ stepwise crushing following the method of Qiu and Dai (1989).

According to the equations of $^{40}\text{Ar}/^{39}\text{Ar}$ geochronology (eq. 2.16, 2.18 of McDougall and Harrison, 1999), a high-precision $^{40}\text{Ar}/^{39}\text{Ar}$ age can be obtained by simply measuring the $^{40}\text{Ar}^*/^{39}\text{Ar}_K$ ratios on an irradiated unknown sample and a reference standard with a high-sensitivity noble gas mass spectrometer.

Stepwise argon extraction techniques (e.g., step heating or crushing) are usually applied in $^{40}\text{Ar}/^{39}\text{Ar}$ dating, and a series of the $^{40}\text{Ar}/^{39}\text{Ar}$ ages can thus be obtained for a single sample. Based on these $^{40}\text{Ar}/^{39}\text{Ar}$ dating data, an age spectrum and an isochron or inverse isochron line can be determined; these

provide more abundant information about the geologic thermal history of the sample in comparison to conventional K-Ar dating method.

Because of the high precision of the $^{40}\text{Ar}/^{39}\text{Ar}$ method and the high sensitivities of the detectors in modern mass spectrometers, K-bearing fluid inclusions in quartz ubiquitously present in most hydrothermal deposits become potential targets for the $^{40}\text{Ar}/^{39}\text{Ar}$ method by progressive crushing. The ores from the Xitian W-Sn polymetallic deposit in central South China possess several minerals suitable for interchronometer comparison, verifying the reliability of dates from the primary fluid inclusions obtained by our $^{40}\text{Ar}/^{39}\text{Ar}$ stepwise crushing technique.

Muscovite, $\text{K}_2\text{Al}_4\text{Si}_6\text{Al}_2\text{O}_{20}(\text{OH}, \text{F})_4$, containing approximately 9.7% K in its structure, is a relatively common mineral in regionally metamorphosed sedimentary rocks, peraluminous granitic rocks, and both pegmatites and hydrothermal veins associated with granitic bodies (McDougall and Harrison, 1999). The argon closure temperature of muscovite is 425°C for grains with a radius of $100 \mu\text{m}$ (Harrison et al., 2009) and 500 – 550°C for grains with a radius of 500 – $1,000 \mu\text{m}$ (Tartese et al., 2011). Warren et al. (2012a, b) used DIFFARG (Wheeler, 1996) to explore the effect of the diffusion data from Harrison et al. (2009) on the retention of Ar in muscovite in

[†]Corresponding author: e-mail, huaningqiu@cug.edu.cn

representative 1.0-, 0.5-, and 0.1-mm-sized grains in the 0- to 3-GPa and 400°–700°C pressure-temperature range, which covers conditions relevant for ^{40}Ar diffusion in metamorphic rocks. Muscovite is one of the best minerals for $^{40}\text{Ar}/^{39}\text{Ar}$ dating because of its high potassium content and good retention of radiogenic argon, which provides a reliable high-precision constraint on the timing of ore formation.

Quartz is the second most abundant mineral in Earth's continental crust and is present in many hydrothermal mineral deposits. Quartz is transparent, and therefore it is easy to observe fluid inclusions contained in it and determine both their homogenization and their freezing temperatures. The fluid inclusions in quartz may have remained closed to argon during postmineralization hydrothermal fluid infiltration. The $^{40}\text{Ar}/^{39}\text{Ar}$ chronometer, based on dating K-bearing fluid inclusions in quartz, will have wide applications in geoscience research. Therefore, we focus on quartz $^{40}\text{Ar}/^{39}\text{Ar}$ crushing in comparison with muscovite $^{40}\text{Ar}/^{39}\text{Ar}$ laser step heating in this study.

Fluid inclusions—especially primary inclusions in minerals—usually behave as closed systems and can be treated as time capsules storing information about ancient geofluids. Noble gases have been useful tools used in the past decades to study fluid inclusions (Villa, 2001; Wilkinson, 2001). Many $^{40}\text{Ar}/^{39}\text{Ar}$ data have been obtained from fluid inclusions hosted in quartz from hydrothermal deposits (Kelley et al., 1986; Turner, 1988; Qiu and Dai, 1989; Turner and Bannon, 1992; Qiu, 1996; Kendrick et al., 2001, 2006; Liu, J., et al., 2015). Previous studies of fluid inclusion $^{40}\text{Ar}/^{39}\text{Ar}$ dating indicate that the progressive crushing technique can yield real ages of the primary fluid inclusions (PFIs), representing mineralization ages, even though the deposits are affected by subsequent hydrothermal activity, resulting in the formation of secondary fluid inclusions (SFIs). We can distinguish SFIs from primary ones on the basis of textural observations (Qiu and Jiang, 2007). The ages of PFIs and SFIs can be distinguished using the $^{40}\text{Ar}/^{39}\text{Ar}$ inverse isochron plot or the K-Cl-Ar correlation plot (Qiu and Jiang, 2007; Jiang et al., 2012; Bai et al., 2013, 2018a, 2019).

Cassiterite (SnO_2), belonging to the rutile group (M^{4+}O_2), is an important ore mineral in most W-Sn deposits. It should have elevated U and low common Pb contents in its crystal structure. It has the ability to preserve U and radiogenic Pb with a high Pb closure temperature of 500°–800°C (Gulson and Jones, 1992; Yuan et al., 2008; Zhang et al., 2014). With the development of more sensitive scientific instrumentation and analytical techniques, low-U minerals have also become suitable for U-Pb dating. Direct cassiterite U-Pb dating has been widely accepted and proven to be a powerful tool in determining ore-forming ages of W-Sn deposits (Yuan et al., 2011; Chen et al., 2014; Zhang, R.Q., et al., 2015, 2017; Li et al., 2016; Carr et al., 2020; Moscati and Neymark, 2020; Slack et al., 2020; Yang et al., 2020).

In this study, the well-constrained mineralization ages are obtained by integrated $^{40}\text{Ar}/^{39}\text{Ar}$ dating of muscovite and quartz samples and laser ablation-inductively coupled plasma-mass spectrometry (LA-ICP-MS) U-Pb dating of cassiterite samples from the Xitian W-Sn polymetallic deposit. These dates indicate that quartz and other nonpotassium minerals that host fluid inclusions containing potassium can be dated

by the $^{40}\text{Ar}/^{39}\text{Ar}$ progressive crushing technique, which will provide a wide application to date various metal mineralization ages.

Geologic Setting

China's tungsten reserves rank first in the world. According to the mineral commodity summaries of the United States Geological Survey (USGS, 2019), China has more than 57% of the world's tungsten reserves and yielded more than 81% of the world's total tungsten production in 2018.

The Xitian W-Sn polymetallic deposit in the eastern Hunan Province in central South China lies at the intersection of the Nanling Range and the Qin-Hang metallogenic belt. The Nanling region in central South China is the most important W-Sn polymetallic province, accounting for more than 92% of the total supply of Chinese tungsten (Liang et al., 2016). Many large-scale W-Sn polymetallic deposits, such as the Shizhuyuan, Furong, Yaogangxian, Xihuashan, and Pangushan deposits, are distributed within the Nanling polymetallic mineralogic region (Fig. 1). Most were formed during the Middle-Late Jurassic (ca. 160–145 Ma) (Hua et al., 2003; Chen, J., et al., 2008, 2013; Hu and Zhou, 2012; Mao, J.W., et al., 2013).

The South China block is composed of the Yangtze block in the northwest and the Cathaysian block in the southeast, which amalgamated along a Neoproterozoic collision belt about 1,000 m.y. ago (Zheng et al., 2013; Zhao et al., 2015). The Yangtze block is comprised of Neoarchean metamorphosed basement, sporadically exposed in the Yunnan, Guizhou, and Hubei provinces (Gao et al., 1999; Qiu and Gao, 2000; Charvet, 2013). The Cathaysian block is composed of Proterozoic basement, Sinian to Triassic sedimentary cover (Chen and Jahn, 1998; Yu et al., 2009; Li et al., 2012), and Mesozoic granitoid intrusions and volcanic rocks covering a total area of ~220,000 km², characterized by extensive metallic mineralization (Zhou et al., 2006).

The Nanling region consists of two Caledonian units, the southern Hunan-eastern Guangxi-northern Guangdong depression in the west and the southern Hunan-southern Jiangxi-Guangdong uplift in the east (Liang et al., 2016). Mid to late Mesozoic (Jurassic, or Yanshanian period) granitic rocks are widespread in the Nanling region. The polymetallic mineralization in this region is always associated with massive late Mesozoic granitic magmatic activity, because nearly all of the polymetallic deposits are located at the endo- and exocontacts of granitic intrusions, and the ore-forming ages are well concordant with the ages of granitic rocks (Zaw et al., 2007; Bai et al., 2013, 2018a, 2019; Liang et al., 2016; Wang et al., 2016; Zhang et al., 2017; Xiao et al., 2019).

The Xitian W-Sn polymetallic deposit, which is located in Zhuzhou City, Hunan Province, central South China, is one of the largest of the deposits discovered during the latest phase of exploration (1999–2011) in the Nanling region, within the Chaling-Chenzhou-Linwu deep fault, a major regional-scale structure whose activity is presumably related to the formation of the deposit (Wang et al., 2003). Granitic magmatism is widespread in the region (Fig. 2). Granitic batholiths consist of Indosinian granites (Late Triassic, 230–215 Ma) and Yanshanian granites (Late Jurassic to Early Cretaceous, 165–141 Ma) (Liang et al., 2016). The Indosinian granites cover

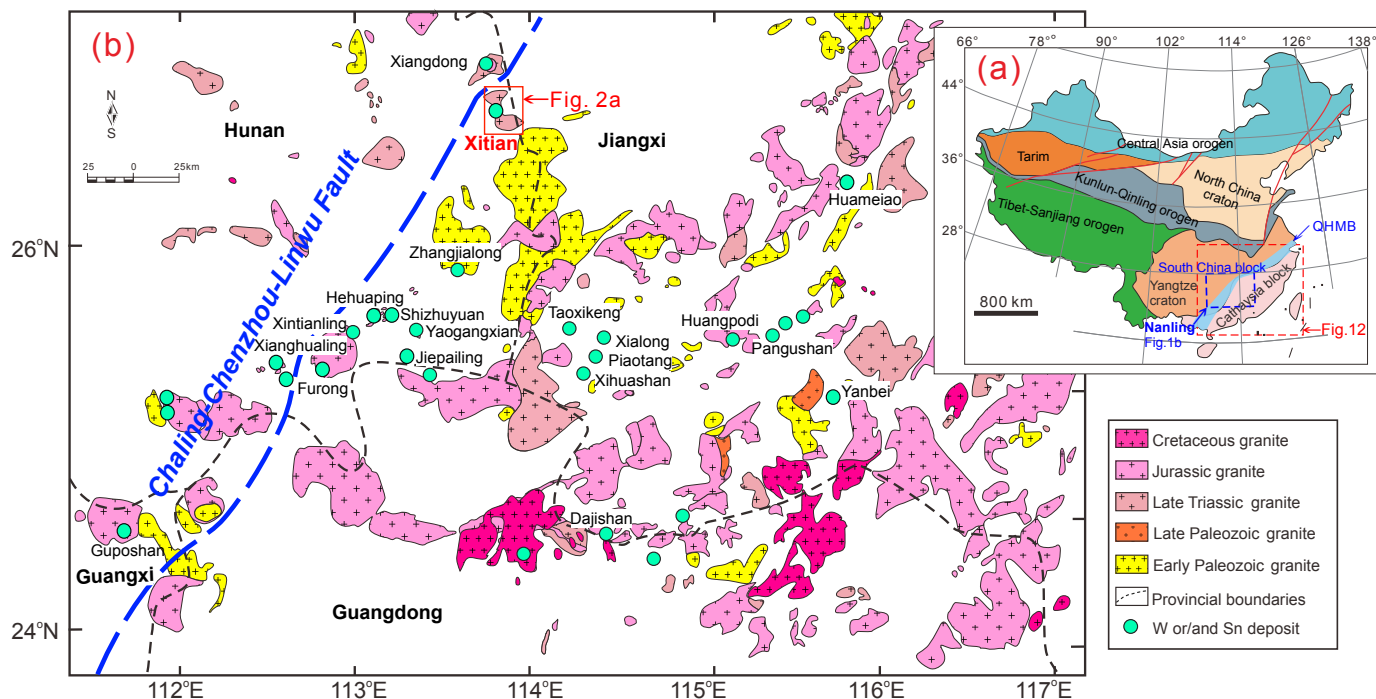


Fig. 1. (a) Tectonic outline of China. (b) Sketch map showing the Yanshanian granites and related tungsten or/and tin deposits in the Nanling Range. QHMB = Qin-Hang metallogenic belt.

the largest outcrop area and are distributed as batholith or stocks. The Yanshanian granites show some typical geochemical signatures of A-type granites and are closely related to W-Sn mineralization. They are scarcely exposed on the surface but interconnected below the surface and intrude into the Indosianian granites as stock or apophyses (Zhou et al., 2015). In the Xitian deposit, W-Sn polymetallic orebodies are comprised of six mining districts: Shaheihe, Heshuxia, Tongmushan, Goudalan, Hualiquan, and Longshang (Fig. 2). The W-Sn mineralization in the area consists of four major types: greisen, skarn, quartz vein, and structurally altered rock types. The cassiterite samples analyzed for U-Pb dating were hand specimens 13XT21, 13XT25, and 13XT30, collected from the Longshang mining district. Mica and quartz samples for $^{40}\text{Ar}/^{39}\text{Ar}$ dating were separated from hand specimens 13XT43, 13XT50, 13XT52, 13XT58, and 13XT79, collected from the Tongmushan mining district, and other samples from the Longshang mining district.

Sampling and Characteristics of Fluid Inclusions

The granite and ore samples were collected from the Tongmushan and Longshang mining districts of the Xitian W-Sn polymetallic deposit (Fig. 3). Single minerals of biotite, muscovite, and quartz aggregates were separated for $^{40}\text{Ar}/^{39}\text{Ar}$ dating, and cassiterite grains were separated for U-Pb dating. Eleven muscovite samples were selected from quartz veins and greisen ores, two biotites from greisen ores, and three biotites from granitic rocks. All the mica grains were fresh (Fig. 4). K-rich muscovite and biotite were analyzed by $^{40}\text{Ar}/^{39}\text{Ar}$ laser stepwise heating, and fluid inclusions in quartz samples were extracted by progressive crushing in vacuo.

Quartz grains from the Xitian W-Sn polymetallic deposit have abundant fluid inclusions. According to the petrography,

microthermometry, and laser Raman spectroscopy, four types of fluid inclusions were recognized in quartz samples: two-phase aqueous inclusions (type I), two- or three-phase CO₂-bearing inclusions (type II), three-phase daughter halite-bearing inclusions (type III), and liquid-only inclusions (type IV) (Fig. 5). Type I and type II fluid inclusions appear in quartz grains that are 3- to 25-μm-sized negative crystals, which are elliptical, elongated, or irregularly shaped, from quartz veins and greisen ores. The homogenization temperatures of type I fluid inclusions range from 200° to 440°C with ice-melting temperatures ranging from -6.3° to -0.8°C, corresponding to salinities of 1.4–9.6 wt % NaCl equiv. Type III fluid inclusions appear in quartz grains that are 10- to 30-μm-sized elliptical-shaped negative crystals from greisen ores. The homogenization temperatures of type III fluid inclusions range from 410° to 470°C with salinities of 31.6–36.7 wt % NaCl equiv (Liu, M., et al., 2015).

Analytical Procedures

$^{40}\text{Ar}/^{39}\text{Ar}$ dating of micas and quartz fluid inclusions

Hand specimens were individually crushed in a stainless-steel mortar and then sieved. The sieved mineral fractions of 30–60 mesh (0.50–0.25 mm) in size were cleaned with deionized water in an ultrasonic bath and then dried in an oven at 120°C. The minerals for $^{40}\text{Ar}/^{39}\text{Ar}$ dating were carefully separated by handpicking under a binocular microscope, then soaked in dilute nitric acid to dissolve carbonate, and then in acetone to remove potential organic materials from the grain surfaces.

The prepared samples were packed in aluminum foil for neutron irradiation together with a neutron fluence monitor, ZBH-25 biotite, packed in copper foil. The Chinese standard samples ZBH-25 biotite, from the Fangshan granodiorite

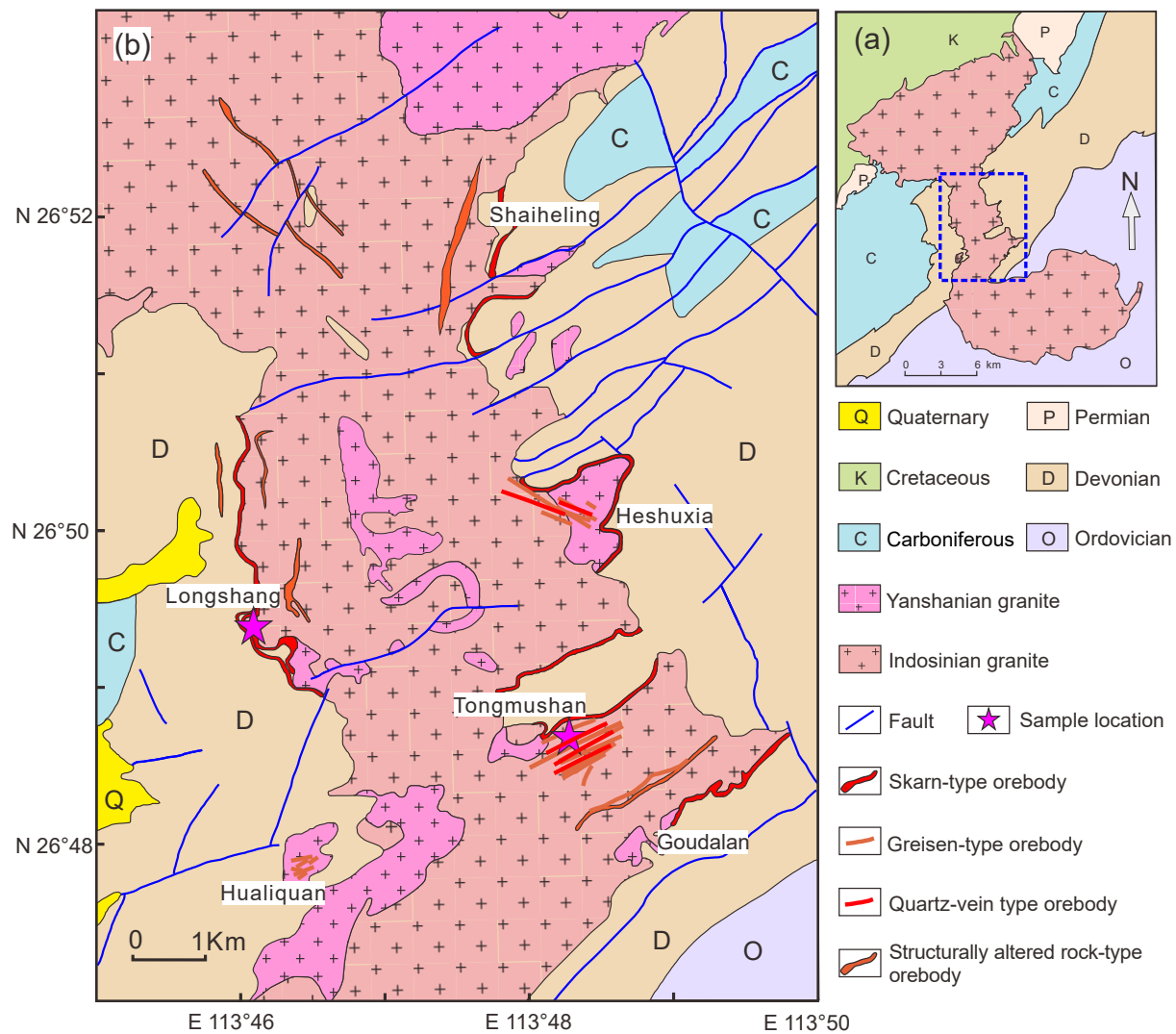


Fig. 2. (a) Simplified map showing the Xitian granites. (b) Simplified geologic map of the Xitian W-Sn polymetallic deposit. Indosinian granites: Late Triassic; Yanshanian granites: Late Jurassic-Early Cretaceous.

complex in southwest Beijing, yielded a K-Ar age of 132.7 ± 1.2 Ma and a flat $^{40}\text{Ar}/^{39}\text{Ar}$ age spectrum with a plateau age of 132.7 ± 0.1 Ma by incremental heating (Wang, 1983).

The $^{40}\text{Ar}/^{39}\text{Ar}$ analyses were performed at the $^{40}\text{Ar}/^{39}\text{Ar}$ laboratory in the China University of Geosciences, using ARGUS VI multicollector noble gas mass spectrometer. The ARGUS VI collector array consists of five Faraday detectors equipped with $10^{11} \Omega$ (H_2), $10^{12} \Omega$ (H_1), and $10^{13} \Omega$ (Ax , L_1 , and L_2) resistors, as well as a low-mass compact discrete dynode (CDD) ion counting multiplier (in the L_3 position). The collector array allows simultaneous collection of five argon isotopes from ^{40}Ar to ^{36}Ar on H_2 to L_2 (for big signal samples) or H_1 to L_3 (for small signal samples). Argon isotopes of samples in this study were collected on H_1 to L_3 . The mass spectrometer has a very low internal volume of about 700 ml, a resolution of >200 , and a sensitivity of 1.45×10^{-3} amps/Torr at $200\text{-}\mu\text{A}$ trap current (Mark et al., 2009; Pfänder et al., 2014). A homemade carbon dioxide infrared laser ($10.6 \mu\text{m}$, 50 W) heating unit was used for stepwise heating. It contained a CCD for sample observation and two cross micromotors to

move the sample chamber in X-Y directions. The irradiated mica samples for laser heating were loaded into sample chambers and degassed at 300°C for 24 h with block flanges, then at 150°C for 72 h with double-vacuum ZnS viewports of 63 mm in diameter mounted on 4½-inch Conflat flanges. An online crusher was directly connected to the purification system to extract fluid inclusions (Qiu and Wijbrans, 2006; Qiu and Jiang, 2007; Qiu et al., 2011; Bai et al., 2018b). The crusher consisted of a stainless-steel tube (height = 160 mm) with a spherical curvature on the internal base ($R = 14.0$ mm), and a magnetic stainless-steel pestle ($R = 13.8$ mm, 222 g). The tube, welded with a DN40CF flange on the top, was connected to the purification line through a bellow. After loading a sample through the flange, the pestle was also moved into the tube's bottom using a permanent strong magnet tool enveloped by a non-magnetic sleeve. The magnet tool is easily separated from the pestle using the sleeve. In order to crush the sample as evenly as possible, two external electromagnets were utilized to hit the crusher tube in a horizontal direction to move the sample grains. The fluid inclusions in K-poor minerals were extracted

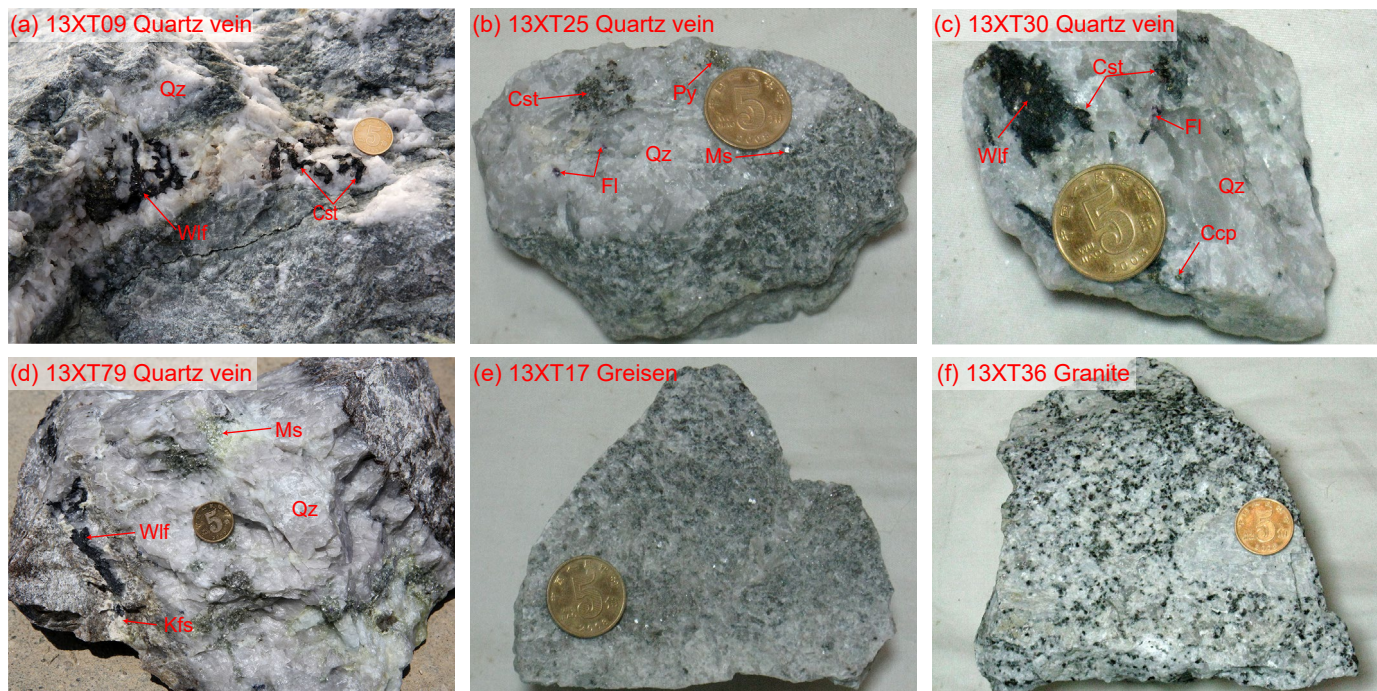


Fig. 3. (a-f) Photographs showing the quartz vein, greisen, and granite samples from the Xitian W-Sn polymetallic deposit. Ccp = chalcopyrite, Cst = cassiterite, Fl = fluorite, Kfs = K-feldspar, Ms = muscovite, Py = pyrite, Qz = quartz, Wlf = wolframite (Whitney and Evans, 2010).

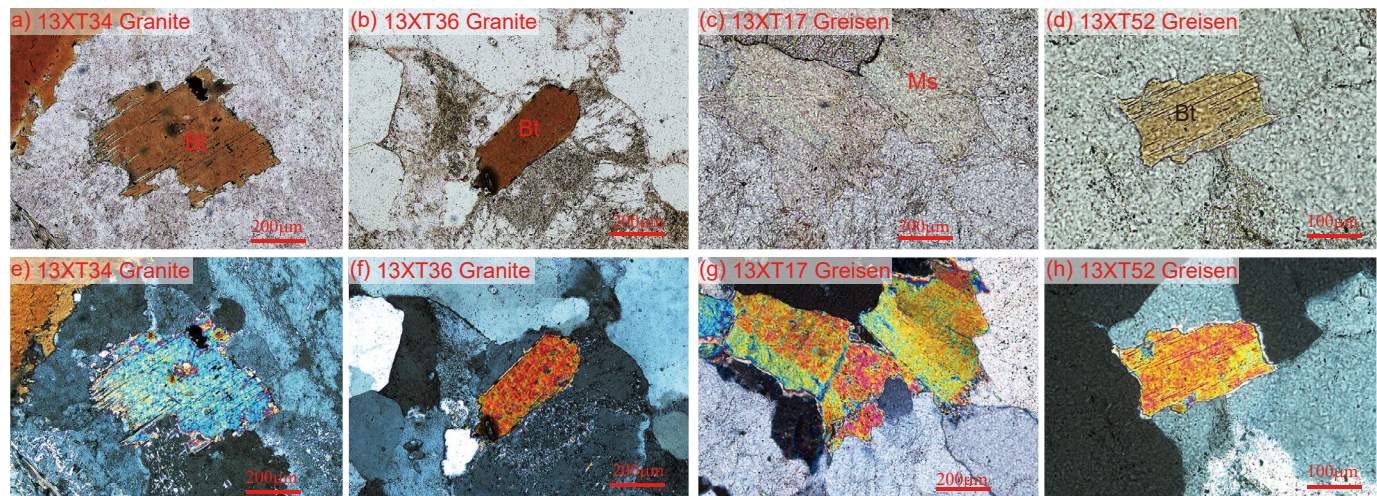


Fig. 4. Photomicrographs of mica in granites and greisen samples from the Xitian W-Sn polymetallic deposit. (a-d) Plane-polarized light. (e-h) Cross-polarized light. Bt = biotite, Ms = muscovite.

by repeatedly lifting and dropping the pestle using an external electromagnet with a frequency of 2 Hz. The pestle was freely falling from a height of 4–5 cm to crush the sample gently (Bai et al., 2018b). The number of pestle drops per extraction step was increased through the experiment to maintain the levels of argon available for analysis. Prior to experiments, the extraction and purification systems were baked out with heat tape, and the sample in the crusher was heated to 150°C with a tube furnace for 10 h to reduce system blanks. In order to correct the system blanks, cool blanks were carried out at the start and end of each sample experiment and between every

four to six steps of sample analyses. Blanks were measured in a static state without the movement of the pestle rather than crushing an empty tube and potentially generating significant amounts of air trapped within the steel (Andrawes et al., 1984; Graney and Kesler, 1995). However, it is noteworthy that the air amount within the steel was significantly low when the crushing was buffered by mineral grains (Blamey, 2012; Xiao et al., 2019). Experiments were terminated when the argon signals were decreased to an obviously low level. A sample was generally crushed for 6,000–20,000 pestle drops, resulting in powder sizes of 1–4 µm (Bai et al., 2013, for 10,245 pestle

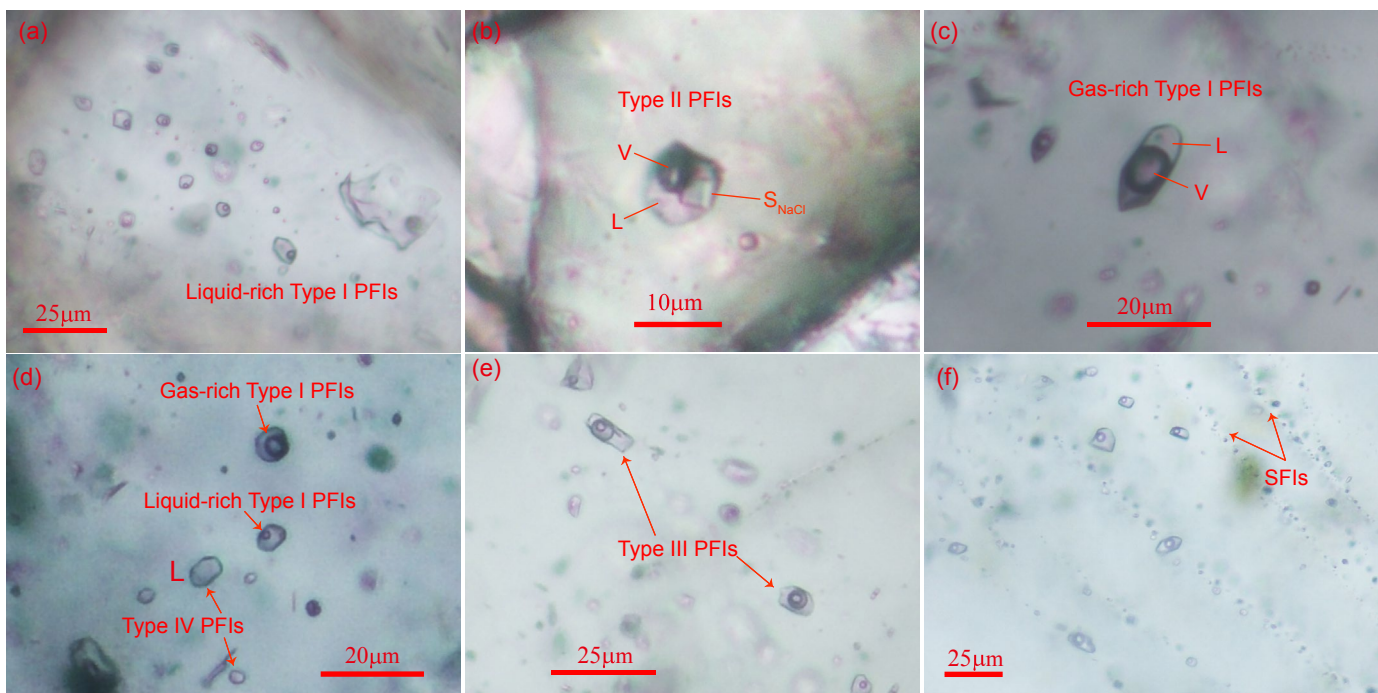


Fig. 5. (a-f) Photomicrographs of typical fluid inclusions in quartz. L = aqueous solution, PFIs = primary fluid inclusions, S = solid, SFIs = secondary fluid inclusions, Type I = two-phase aqueous inclusions, Type II = two or three-phase CO₂-bearing inclusions, Type III = three-phase daughter halite-bearing inclusions, Type IV = liquid-only inclusions, V = vapor phase.

drops) and releasing most fluid inclusions. After the experiment, the crusher tube was disconnected from the line at the flange. The tube, including the pestle inside, was filled with deionized water and cleaned in an ultrasonic bath for 30 min. The powders were rinsed with deionized water into a big plastic bottle. The wet tube and pestle were wiped with kim-wipes and dried in a furnace at 150°C for 1 h before loading a new sample.

Neutron irradiation and correction factors: Neutron irradiation for ⁴⁰Ar/³⁹Ar dating has been a serious problem for a decade in China. Under a key project from the National Natural Science Foundation of China (NSFC), we have established a new irradiation collaboration with the group from China Mianyang Research Reactor (CMRR) for the Earthtime-CN. The samples were irradiated for 30 h in the CMRR reactor. Argon isotopes derived from Ca and K are determined by measuring the relative production rates of these isotopes in pure calcium salt (CaF₂) and potassium salt (K₂SO₄) after neutron irradiation. The salts irradiated in the CMRR reactor were analyzed on the ARGUS VI. The correction factors (³⁶Ar/³⁷Ar)_{Ca} and (³⁹Ar/³⁷Ar)_{Ca} from the irradiated CaF₂ are 2.3477×10^{-4} and 6.1748×10^{-4} , respectively, and the correction factors (⁴⁰Ar/³⁹Ar)_K and (³⁸Ar/³⁹Ar)_K from the irradiated K₂SO₄ are 2.3228×10^{-3} and 9.4194×10^{-3} , respectively (Bai et al., 2018b).

LA-ICP-MS cassiterite U-Pb dating

Uranium-lead isotope analyses of cassiterites from the Xitian W-Sn deposit were carried out using the LA-ICP-MS system in the CAS Key Laboratory of Mineralogy and Metallogeny, Guangzhou Institute of Geochemistry, Chinese Academy of Sciences (CAS). The system consists of an Agilent 7900

ICP-MS coupled with a Resonetics RESOlution S-155 laser (Li et al., 2016; Zhang et al., 2017). Cassiterite grains were analyzed using a laser energy density of 4 J/cm², a spot size of 74 µm, and a repetition rate of 6 Hz. NIST SRM 610 and an in-house cassiterite standard, AY-4, were used as external elemental and isotopic calibration standards, respectively. AY-4 was collected from the Anyuan skarn-type tin deposit of the Furong tin ore field in the Middle Nanling Range. This cassiterite U-Pb age of 158.2 ± 0.4 Ma has been well constrained by the isotope dilution-thermal ionization mass spectrometry (ID-TIMS) technique (Yuan et al., 2011). NIST SRM610 was analyzed twice every 12 analyses of unknown samples. AY-4 was analyzed twice every six analyses of the unknown samples.

Analytical Results

Cassiterite U-Pb age

The cassiterite U-Pb data are listed in Appendix 1. Raw data reduction was performed by ICPMSDataCal software (Liu et al., 2008, 2010), including the integration of background and analysis signals, time-drift correction, and quantitative calibration for trace elements. The U-Pb ages and concordia diagrams were obtained with Isoplot 4.15 (Ludwig, 2008). Uncertainties of single spot isotopic analyses were 1σ , and the weighted mean ²⁰⁶Pb/²³⁸U ages were quoted at the 95% confidence level.

Cassiterite grains were collected from three hand specimens, 13XT21, 13XT25, and 13XT30, from the Longshang mining district of the Xitian W-Sn polymetallic deposit. Ore samples were crushed to 20–60 mesh. Cassiterite grains were handpicked under a binocular microscope, mounted in epoxy, and then polished down to near-half sections to expose

internal structures. The cassiterite grains have abundant cracks and most show clear and bright oscillatory zonation in cathodoluminescence (CL) images (Fig. 6b). Most cassiterite grains from the Xitian deposit have abundant fluid inclusions (Fig. 6c), which is a feature often associated with high concentrations of common Pb (Li et al., 2016). Therefore, the U-Pb isotope analyses were conducted on the cassiterite grains with bright CL images and clear zonation, avoiding cracks and fluid inclusions. When the fluid inclusions were ablated, the U and Pb isotope intensities would be abnormally high or low, and these abnormal data were ignored.

Chew et al. (2014) suggested that an approach often employed in U-Pb dating of high common Pb phases, such as the LA-ICP-MS U-Pb dating studies of titanite (Simonetti et al., 2006) and apatite (Chew et al., 2011), involves projecting a straight line through the uncorrected data on a Tera-Wasserburg concordia to determine the common Pb component (y -intercept) on the $^{207}\text{Pb}/^{206}\text{Pb}$ axis. Li et al. (2016) proposed that common Pb has less influence on the Tera-Wasserburg ages; in other words, an inverse (Tera-Wasserburg) concordia diagram is the best way to reduce common Pb effects.

Thirty-six spots on 24 cassiterite grains from sample 13XT21 were measured. The ^{238}U and common Pb concentrations are 1.27–78.1 ppm and 0–0.56 ppm, respectively. The analysis

data yield a U-Pb concordia lower intersection age of 151.5 ± 1.7 Ma (mean square of weighted deviates [MSWD] = 0.54) and a U-Pb Tera-Wasserburg lower intersection age of 151.6 ± 1.6 Ma (MSWD = 0.52), excluding some deviated points (Fig. 7a, b).

Thirty-six spots on 22 cassiterite grains from sample 13XT25 were measured. The ^{238}U and common Pb concentrations are 0.92–50.8 ppm and 0–0.39 ppm, respectively. The analysis data yield a U-Pb concordia lower intersection age of 149.7 ± 2.1 Ma (MSWD = 0.65) and a U-Pb Tera-Wasserburg lower intersection age of 149.5 ± 2.2 Ma (MSWD = 0.69) (Fig. 7c, d).

Thirty-six spots on 26 cassiterite grains of sample 13XT30 were measured. The ^{238}U and common Pb concentrations are 1.49–140 ppm and 0–0.58 ppm, respectively. The analysis data yield a U-Pb concordia lower intersection age of 151.7 ± 2.1 Ma (MSWD = 0.51), and a U-Pb Tera-Wasserburg lower intersection age of 151.8 ± 1.8 Ma (MSWD = 0.52) (Fig. 7e, f).

$^{40}\text{Ar}/^{39}\text{Ar}$ age spectra and isochrons

The $^{40}\text{Ar}/^{39}\text{Ar}$ data are listed in Appendices 2 and 3. The $^{40}\text{Ar}/^{39}\text{Ar}$ results were calculated and plotted using the software ArArCALC v.2.5.2.

In the present study, 16 mica samples (10 muscovite samples and six biotite samples) were analyzed by laser step heating

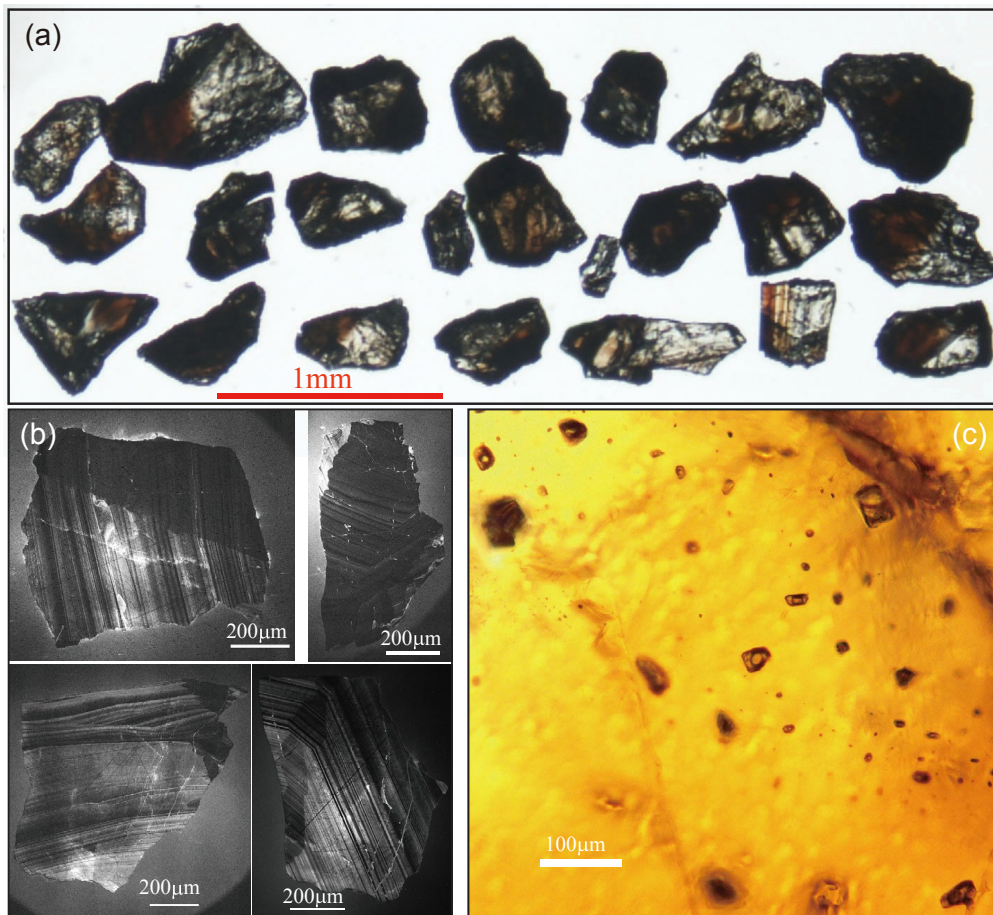


Fig. 6. Cassiterite grains from the Xitian W-Sn polymetallic deposit. (a) Transmission image for the cassiterite grains from the quartz veins. (b) Cathodoluminescence images of representative cassiterite grains analyzed by laser ablation-inductively coupled plasma-mass spectrometry dating. (c) Photomicrograph showing the fluid inclusions (FIs) in cassiterite. When the FIs were ablated, the U and Pb isotope intensities would be abnormally high or low and abandoned.

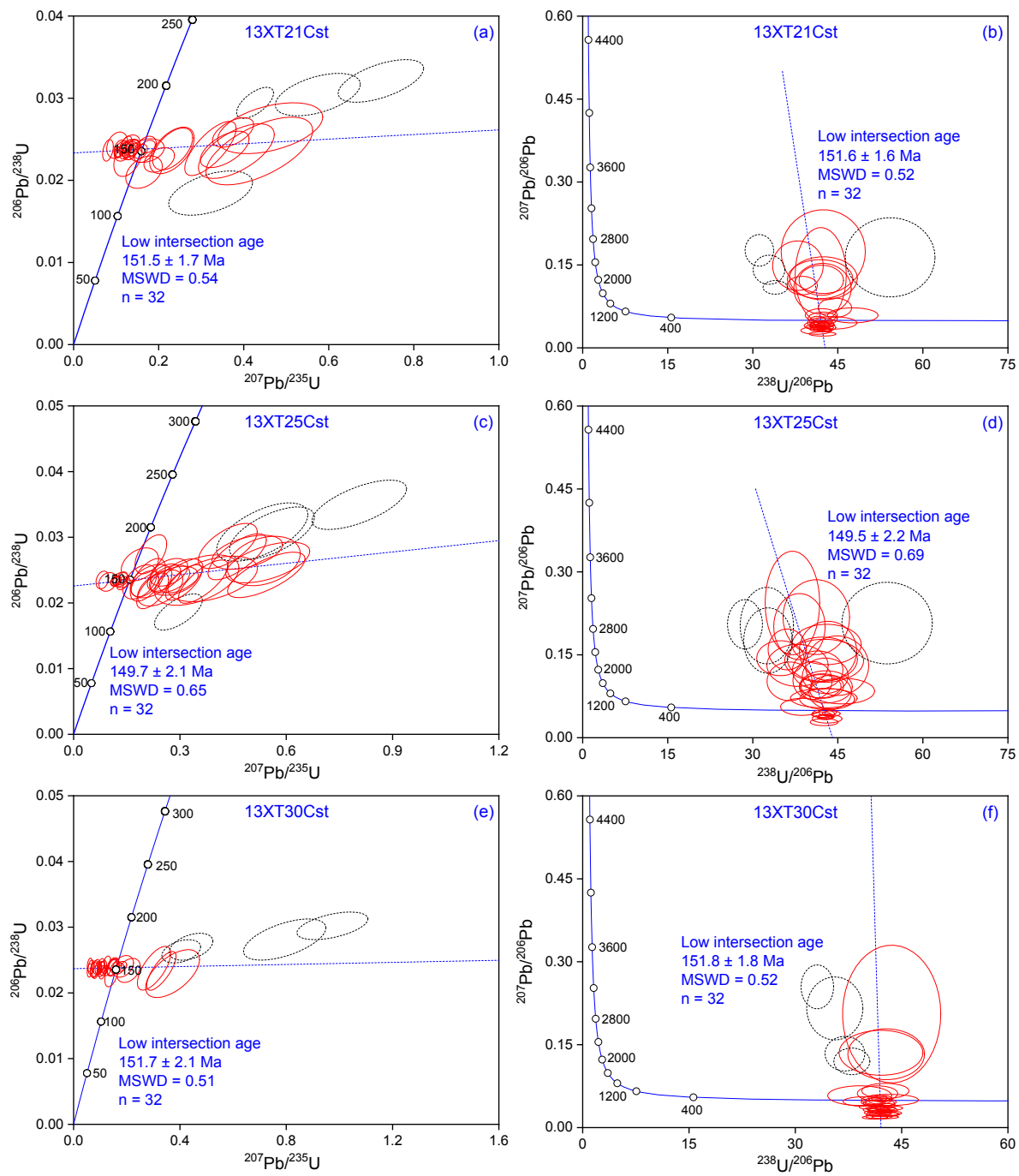


Fig. 7. (a-f) Diagrams of concordia (left) and Tera-Wasserburg concordia (right) for cassiterite laser ablation-inductively coupled plasma-mass spectrometry U-Pb dating. The lower intersection ages of concordia and Tera-Wasserburg diagrams are identical for each sample. (Laser beam: $\phi 74 \mu\text{m}$; energy density: 4 J/cm^2 ; repetition rate of 6 Hz. Dark dotted data points are excluded from the age calculations.) MSWD = mean square of weighted deviates.

(App. 2) and nine quartz samples by progressive crushing (App. 3). The age spectra of the $^{40}\text{Ar}/^{39}\text{Ar}$ dating results of the micas are shown in Figure 8. The age spectra and inverse isochron plots of the nine quartz samples are shown in Figures 9 and 10. All the analysis errors are 2σ . Hand specimens 13XT43, 50, 52, 58, and 13XT79 were collected from the Tongmushan mining district; others were collected from the Longshang mining district.

“Age plateau” is important terminology of the $^{40}\text{Ar}/^{39}\text{Ar}$ geochronology, which was advanced by many schemes since the first proposal by Dalrymple and Lanphere (1974). Recently Schaen et al. (2021) resuggested that a plateau (1) consists of at least five or more consecutive steps that comprise at least $>50\%$ of the ^{39}Ar released, (2) does not have a slope, and (3) yields an isochron regressed through all of the plateau steps with a $(^{40}\text{Ar}/^{36}\text{Ar})_i$ that is indistinguishable from the

atmospheric value at the 95% confidence level (for terrestrial samples only). In this study, all the mica samples dated by $^{40}\text{Ar}/^{39}\text{Ar}$ laser stepwise heating form very flat age spectra with very concordant plateau and isochron ages. The 16 mica samples have a narrow $^{40}\text{Ar}/^{39}\text{Ar}$ age range from 152.4 to 148.1 Ma with an average of 150.2 ± 0.6 Ma. These high-precision $^{40}\text{Ar}/^{39}\text{Ar}$ ages of micas constrain the W-Sn mineralization ages in Xitian.

When interpreting the $^{40}\text{Ar}/^{39}\text{Ar}$ age spectra for the Jurassic Atlantic continental tholeiites of Guyana, Deckart et al. (1997, p. 211) indicated that “the age spectra display a relatively flat region ... corresponding to 20–49% of total released ^{39}Ar and showing three to five concordant successive apparent ages,... from now on referred to as ‘mini-plateau ages.’”

The term “mini-plateau” is also very important for the $^{40}\text{Ar}/^{39}\text{Ar}$ stepwise crushing technique because the argon reservoirs may be from SFIs, PFIs, and possible micrometer-scale K minerals, as well as a mixture of all these features. For the cases of multiargon reservoirs, we suggest the following:

1. A mini-plateau consists of four or more consecutive steps clearly defining an inverse isochron line.
2. When the initial $(^{40}\text{Ar}/^{36}\text{Ar})_0$ ratio corresponding to the inverse isochron line is applied to exclude the nonradioactive ^{40}Ar from these steps, their ages will be concordant with the inverse isochron age and yield a mini-plateau.
3. The ^{39}Ar amount might sometimes be less than 20% of total released ^{39}Ar .
4. The $(^{40}\text{Ar}/^{36}\text{Ar})_0$ might represent the trapped argon or a mixing gas ratio (Bai et al., 2018a).

Age spectra of the nine quartz samples dated by $^{40}\text{Ar}/^{39}\text{Ar}$ progressive crushing show two different $^{40}\text{Ar}/^{39}\text{Ar}$ release patterns: 13XT21Q, 23Q, 42Q, and 79Q form saddle-shaped age spectra, while 13XT08Q, 09Q, 17Q, 34Q, and 52Q yield declining age spectra marked by abnormally old apparent ages in the first several steps, then decrease remarkably during subsequent steps and finally form flat (mini-) plateaus (Fig. 9). The mini-plateau ages of 13XT08Q, 09Q, and 17Q are 152.1 ± 1.5 (MSWD = 0.46, $\Sigma^{39}\text{Ar} = 48.36\%$), 151.4 ± 1.9 (MSWD = 0.09, $\Sigma^{39}\text{Ar} = 34.75\%$), and 150.8 ± 1.5 Ma (MSWD = 0.33, $\Sigma^{39}\text{Ar} = 28.48\%$), respectively, whereas sample 13XT34Q yields a plateau age of 151.8 ± 1.5 Ma (MSWD = 0.30, $\Sigma^{39}\text{Ar} = 62.68\%$). On the inverse isochron plot of $^{36}\text{Ar}/^{40}\text{Ar}$ versus $^{39}\text{Ar}/^{40}\text{Ar}$ (Fig. 10), the data points corresponding to the plateaus yield inverse isochron ages of 152.0 ± 1.6 , 151.9 ± 3.1 , 151.0 ± 2.5 , and 152.0 ± 1.5 Ma, with initial $^{40}\text{Ar}/^{36}\text{Ar}$ ratios of 299.6 ± 7.3 , 298.1 ± 2.1 , 297.8 ± 11.4 , and 296.2 ± 4.0 , respectively, which are indistinguishable from the modern atmospheric $^{40}\text{Ar}/^{36}\text{Ar}$ ratio of 298.56 (Lee et al., 2006). The final steps (steps 11–19) of 13XT52Q have a wide range of $^{40}\text{Ar}/^{39}\text{Ar}$ apparent ages varying from 191.2 to 178.0 Ma. These data points yield a well-defined isochron with an age of 150.2 ± 12.3 Ma, corresponding to an initial $^{40}\text{Ar}/^{36}\text{Ar}$ ratio of 325.6 ± 9.7 , which implies the existence of a little excess ^{40}Ar . A flat plateau is obtained for steps 11–19 with a plateau age of 150.2 ± 2.2 Ma when we excluded the nonradioactive ^{40}Ar with the initial $^{40}\text{Ar}/^{36}\text{Ar}$ ratio (325.6) from the inverse isochron plot.

Inverse isochron lines corresponding to the initial steps are also obtained for samples 13XT08Q (steps 4–13), 13XT52Q (steps 5–10), 13XT17Q (steps 5–11), 13XT09Q (steps 6–11),

and 13XT34Q (steps 5–14) with young ages of 85.9 ± 1.2 , 87.5 ± 5.9 , 127.1 ± 1.8 , 142.0 ± 3.6 , and 142.7 ± 1.4 Ma, respectively, corresponding to $^{40}\text{Ar}/^{36}\text{Ar}$ initial ratios of 732.4 ± 3.4 , 423.8 ± 3.2 , 706.7 ± 4.9 , 344.7 ± 2.5 , and 430.0 ± 2.2 , which are much higher than the 298.56 ratio of modern atmosphere (Lee et al., 2006), indicating obvious excess ^{40}Ar ($^{40}\text{Ar}_{\text{e}}$) inside the SFIs of these samples.

The quartz samples 13XT21Q, 23Q, 42Q, and 79Q form saddle-shaped age spectra, with youngest apparent ages still much older than the mica $^{40}\text{Ar}/^{39}\text{Ar}$ plateau ages of 152.4–148.1 Ma. On the inverse isochron plots of $^{36}\text{Ar}/^{40}\text{Ar}$ versus $^{39}\text{Ar}/^{40}\text{Ar}$, data points from steps 4–19 of 13XT21Q, steps 5–17 of 13XT79Q, and steps 8–17 of 13XT23Q yield isochrons with ages of 153.7 ± 6.1 , 151.7 ± 5.1 , and 149.9 ± 8.5 Ma, corresponding to $^{40}\text{Ar}/^{36}\text{Ar}$ initial ratios of 380.7 ± 2.0 , 528.2 ± 4.2 , and 319.0 ± 2.4 , respectively, which are also higher than the atmospheric value of 298.56 (Lee et al., 2006), indicating some excess ^{40}Ar in the final crushing steps. Their flat plateaus are obtained from the steps, which define isochron lines with ages of 153.8 ± 3.4 (MSWD = 0.23, $\Sigma^{39}\text{Ar} = 96.37\%$), 151.6 ± 3.0 (MSWD = 0.09, $\Sigma^{39}\text{Ar} = 93.50\%$), and 149.8 ± 3.7 Ma (MSWD = 0.10, $\Sigma^{39}\text{Ar} = 39.83\%$). This was done by excluding the nonradiogenic ^{40}Ar based on their initial $^{40}\text{Ar}/^{36}\text{Ar}$ ratios from the inverse plots, which are indistinguishable from their isochron ages.

The inverse isochron plot based on the data points from sample 13XT42Q defines two isochron lines. One line is defined by the data points from steps 13–24 with an age of 152.1 ± 2.2 Ma, corresponding to an initial $^{40}\text{Ar}/^{36}\text{Ar}$ ratio of 493.8 ± 3.3 . The other line is defined by the data points from steps 4–11 yielding an age of 119.0 ± 1.6 Ma with an initial $^{40}\text{Ar}/^{36}\text{Ar}$ ratio of 811.8 ± 3.9 . If the initial $^{40}\text{Ar}/^{36}\text{Ar}$ ratios of each of the two isochrons are applied to exclude their nonradiogenic ^{40}Ar , a plateau and a mini-plateau are obtained for the steps 4–11 and steps 13–24 with ages of 119.0 ± 2.0 (MSWD = 0.64, $\Sigma^{39}\text{Ar} = 58.28\%$) and 152.1 ± 1.6 Ma (MSWD = 0.39, $\Sigma^{39}\text{Ar} = 31.02\%$), respectively.

Discussion

Flat age spectra of mica

Muscovite is one of the best minerals for $^{40}\text{Ar}/^{39}\text{Ar}$ dating because of its high potassium content and good retention of radiogenic argon, providing a reliable constraint on the ore-forming ages.

Muscovite and biotite commonly yield essentially flat age spectra when undisturbed. Muscovite has a higher closure temperature than biotite, when considering Ar loss via thermally driven volume diffusion. During alteration, muscovite, although not unalterable, is much more resistant to change than biotite. The chemical nature of the alteration process of both micas is held to be essentially a replacement of potassium by hydrogen. In the case of altered biotite, potassium, magnesium, and iron decrease, while alumina, silica, and water increase (Denison et al., 1929).

Eleven muscovite samples were selected from the quartz veins and greisen ores, two biotites from the greisen ores, and three biotites from the granitic rocks. All the mica grains were fresh (Fig. 4). The ore muscovite $^{40}\text{Ar}/^{39}\text{Ar}$ plateau ages are 151.8 – 148.1 Ma with an average of 149.9 ± 0.6 Ma, the

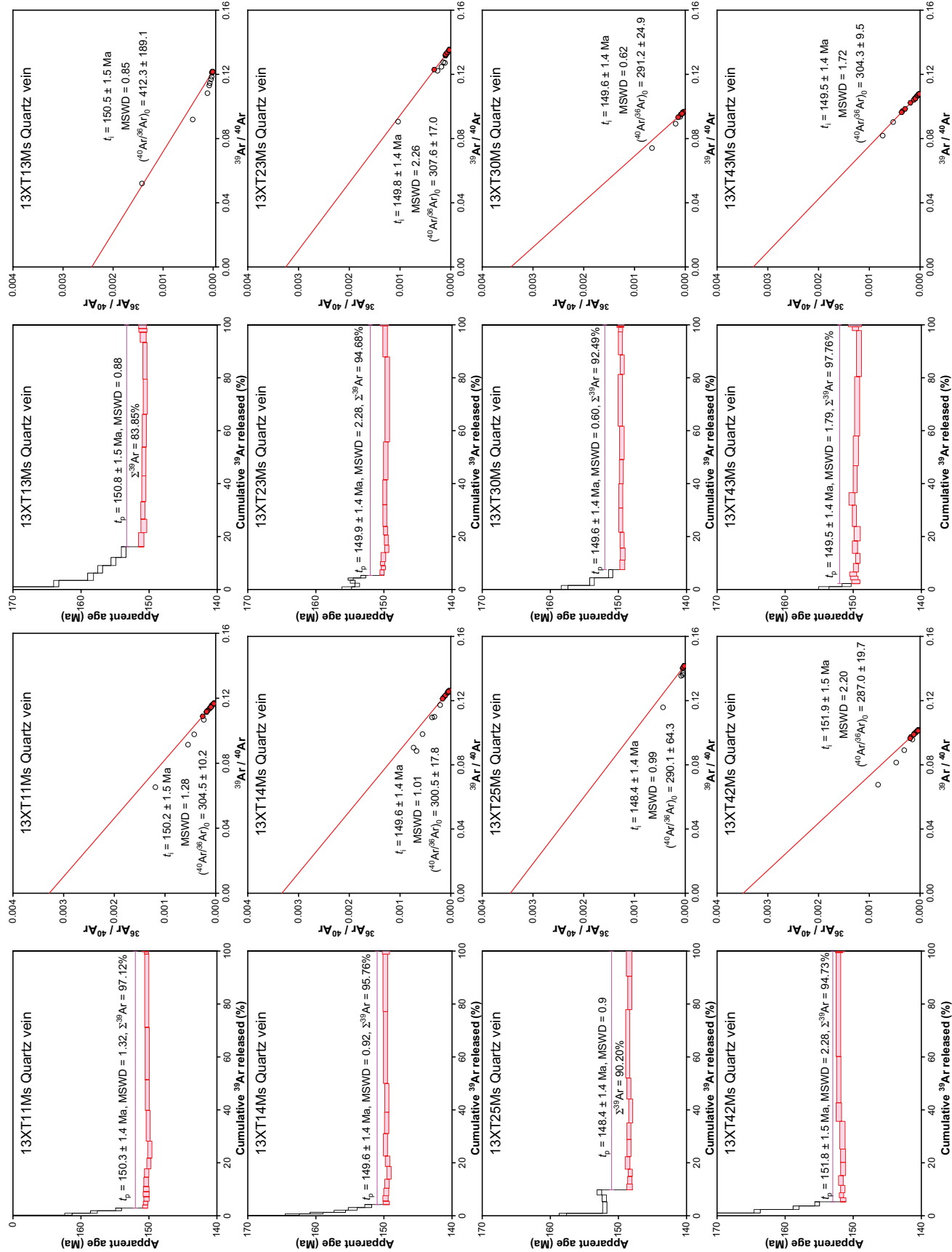


Fig. 8. Laser stepwise heating $^{40}\text{Ar}/^{39}\text{Ar}$ age spectra and inverse isochrons for mica samples from the Xitian W-Sn polymetallic deposit. t_i = inverse isochron ages, t_p = plateau ages. MSWD = mean square of weighted deviates.

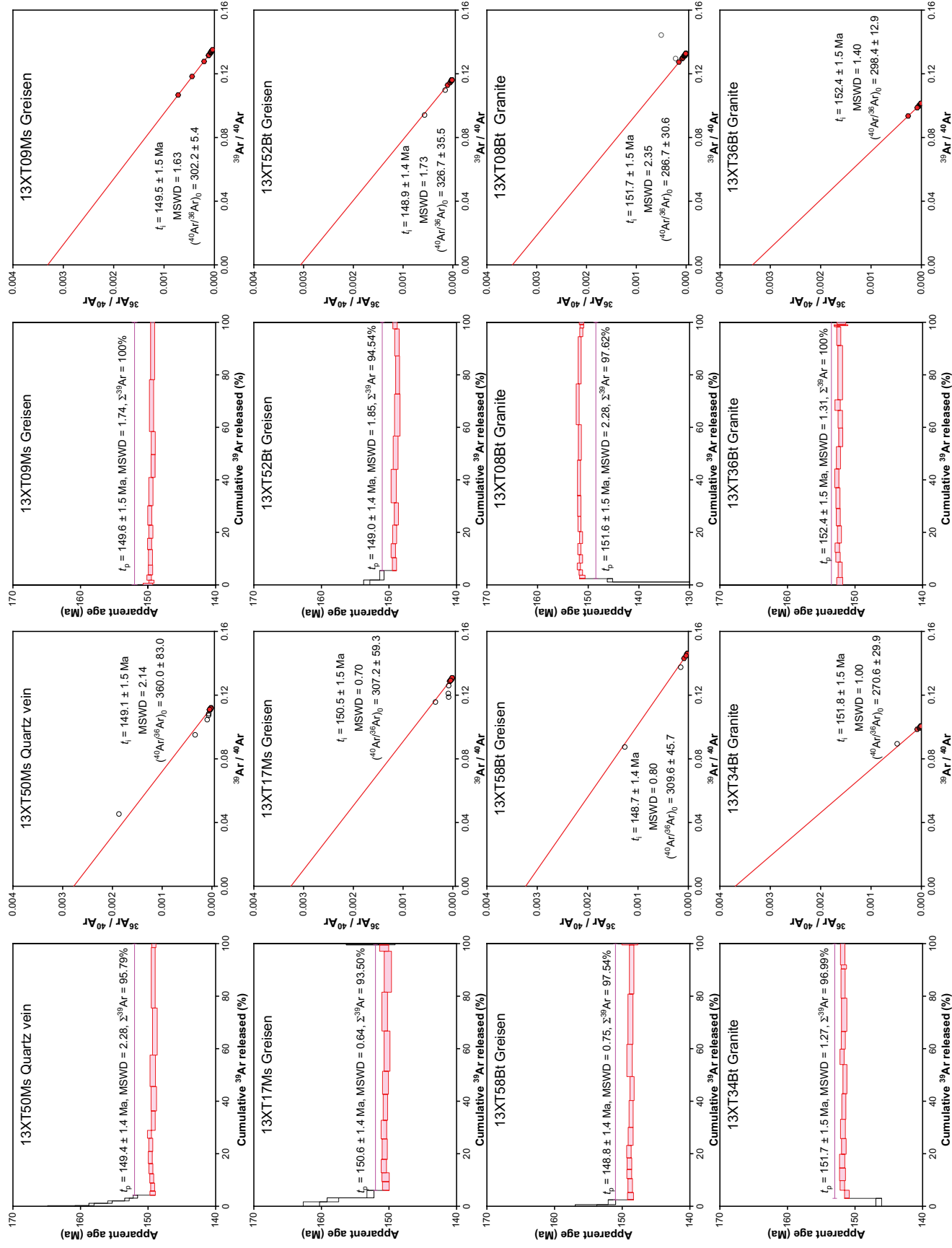


Fig. 8. (Cont.)

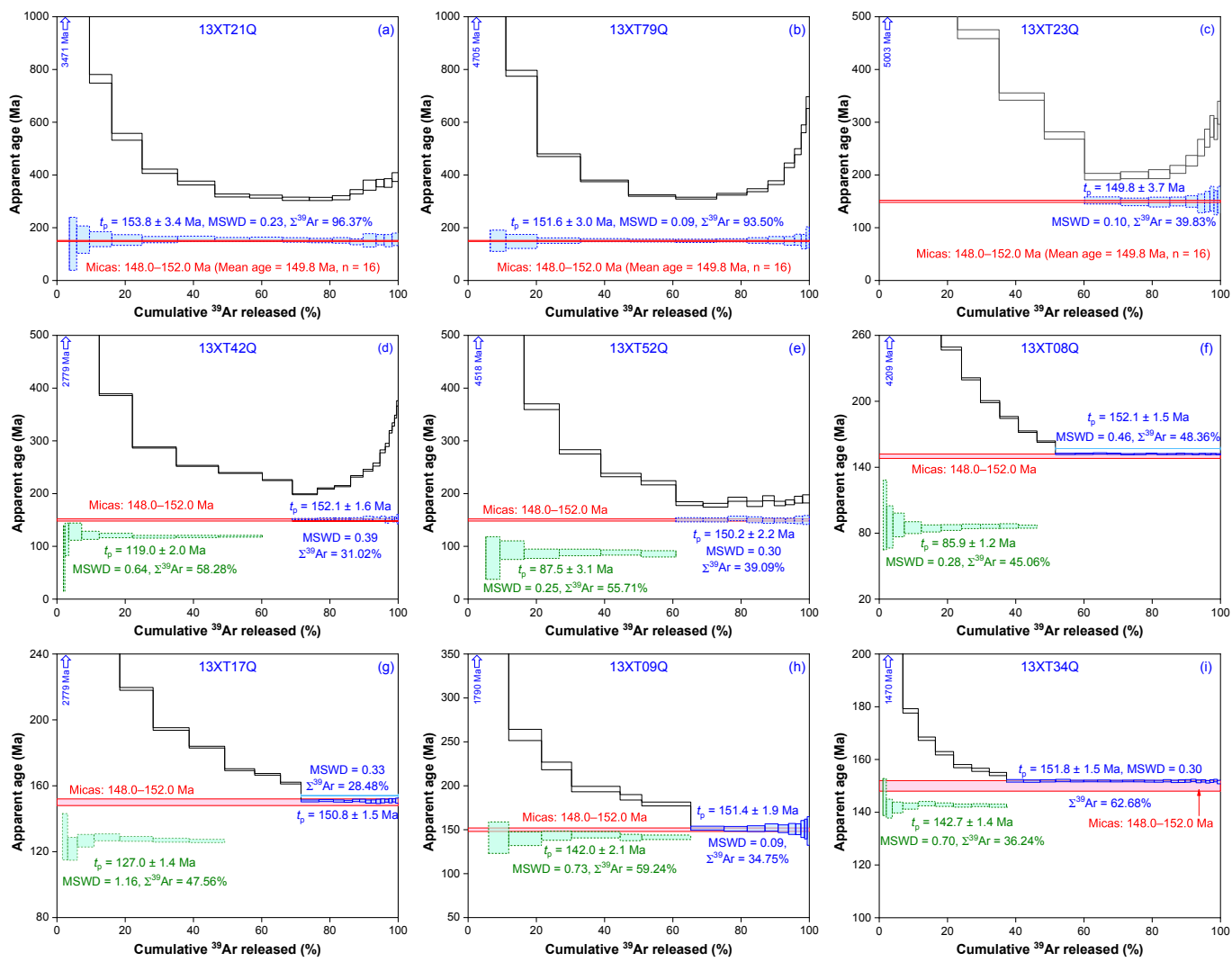


Fig. 9. (a-i) Stepwise crushing $^{40}\text{Ar}/^{39}\text{Ar}$ age spectra for quartz samples, in comparison to the red age range of 152.0–148.0 Ma of the mica samples shown in Figure 8. The quartz apparent ages in dark solid lines are obtained by excluding non-radiogenic ^{40}Ar with modern atmospheric $^{40}\text{Ar}/^{36}\text{Ar}$ ratio of 298.56, while the (mini-)plateau ages (t_p) in dashed lines are calculated by applying the initial $(^{40}\text{Ar}/^{36}\text{Ar})_0$ ratios of the inverse isochrons (Fig. 10) to exclude nonradiogenic ^{40}Ar . The green steps correspond to the secondary fluid inclusions and the blue steps to the primary fluid inclusions. MSWD = mean square of weighted deviates.

greisen biotite ages are 149.0–148.8 Ma with an average of $148.9 \pm 1.0 \text{ Ma}$, and the granitic biotite ages are 152.4–151.6 Ma with an average of $151.9 \pm 0.9 \text{ Ma}$. All the mica ages are indistinguishable within the analytical uncertainties, suggesting that the W-Sn hydrothermal mineralization occurred soon after the granite cooled down to the biotite closure temperature of 300°–350°C.

It should be noted that altered biotites might yield a younger age than mineralization even if they have a flat age spectrum. It is therefore very important to analyze very fresh biotite grains.

Cassiterite U-Pb ages

Cassiterite (SnO_2) is an important ore mineral of W-Sn polymetallic deposits, crystallizing from the ore-forming fluid during an early stage of mineralization. Therefore, direct dating

of cassiterite will provide firm constraints on the relationship between magmatism and hydrothermal mineralization, especially coupled with other dating methods (Li et al., 2016). In this study, the cassiterite grains selected from three quartz-vein ores (13XT21, 25, and 30) yield a tight U-Pb age range of 151.7–149.7 Ma with an average of $151.1 \pm 1.1 \text{ Ma}$, which is concordant with the ore muscovite average $^{40}\text{Ar}/^{39}\text{Ar}$ age of $149.9 \pm 0.6 \text{ Ma}$ within analytical uncertainties. These concordant mica $^{40}\text{Ar}/^{39}\text{Ar}$ and cassiterite U-Pb ages define the ore-forming ages for the Xitian W-Sn deposit.

Crushing technique and gas reservoirs

Before discussing the $^{40}\text{Ar}/^{39}\text{Ar}$ dating results by crushing, we further clarify our crushing technique and summarize the gas release sequence from the reservoirs. Our crushing technique should be described as the following:

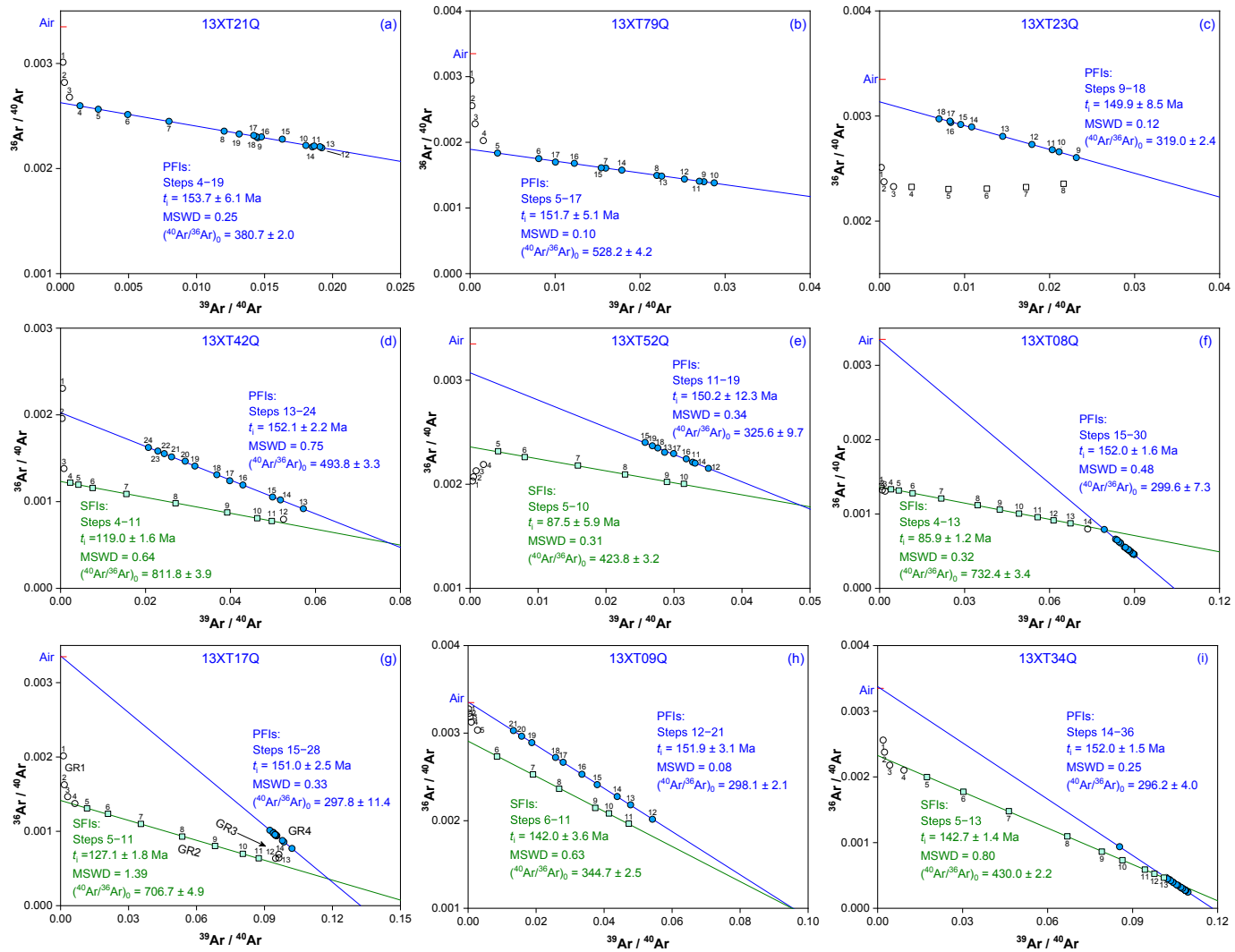


Fig. 10. (a-i) $^{40}\text{Ar}/^{39}\text{Ar}$ inverse isochrons for quartz samples by stepwise crushing. The green points and lines are interpreted as the secondary fluid inclusions (SFIs) and the blue ones as the primary fluid inclusions (PFIs). The $(^{40}\text{Ar}/^{36}\text{Ar})_0$ of all SFIs and most PFIs are obviously higher than the modern atmospheric value of 298.56, indicating that the fluids from the deep crust and the relatively closed environments keep the excess ^{40}Ar from escaping. Some PFI isochron $(^{40}\text{Ar}/^{36}\text{Ar})_0$ ratios close to the modern atmospheric value might imply that the open environments release the excess ^{40}Ar during mineralization. MSWD = mean square of weighted deviates.

1. Stepwise: The extraction steps are usually near 20 or more.
2. Gentle: The pestle weighing ~220 g is lifted up 4–5 cm and then freely falls down to hit the sample grains gently. The hitting pressure is about 1.5 psi.
3. Progressive: The pestle drop number increases step by step from tens in the first step to hundreds (such as 10, 20, 40, ..., 400, 500, 600, 700, 800, ..., 800) subsequently, to maintain sufficient gas for measurement. We tried our best for the initial steps to be sets of 10 hits in order to increase the possibility of obtaining isochron ages from SFIs.
4. Uniform particle size by horizontal hitting: While the pestle is moving vertically inside the tube, two other external pestles are moving horizontally to hit the tube's bottom end from the opposite sides, moving the fine grains. If the grains stay in their positions without horizontal hitting, the resulting grain sizes will be bigger moving away from the

tube's bottom center. Horizontal hitting causes a more uniform sample particle size during a crushing experiment.

It is reasonable that the mineral grains will be preferentially broken along microcracks by crushing. As the crushing experiment proceeds, gas reservoirs are released in the following sequence and can be recognized as the groups of the data points (GR) on the $^{40}\text{Ar}/^{39}\text{Ar}$ inverse isochron plots (Fig. 10g) (Qiu and Jiang, 2007; Qiu and Wijbrans, 2008; Jiang et al., 2012; Bai et al., 2019; Xiao et al., 2019):

1. GR1: Gases trapped in microcracks usually containing some excess ^{40}Ar and extremely low potassium; these gases are inferred to be from deep degassing after the SFIs;
2. GR2: SFIs with excess ^{40}Ar distributed along the healed microcracks, probably yielding an SFI inverse isochron line;

3. GR3: Mixture from the SFIs to PFIs;
4. GR4: Micrometer-sized isolated PFIs, usually yielding a PFI inverse isochron line;
5. GR5: Mixture from PFI and SFI components (fluids and/or solid minerals), probably yielding a gas mixing line (Bai et al., 2013, 2018a);
6. GR6: Micro- to nanometer-sized solid minerals (if present), released by prolonged crushing.

The gas release sequence with sufficient crushing can be summarized as from microcracks → SFIs → PFIs → micrometer- to nanometer-sized minerals. Xiao et al. (2019) verified the gas release sequence through integrated studies on fluid inclusions using Raman spectroscopy, quadrupole mass spectrometry gas composition, and $^{40}\text{Ar}/^{39}\text{Ar}$ stepwise crushing. The host minerals included wolframite, cassiterite, and quartz from the Yaogangxian tungsten deposit in south Hunan Province (Fig. 1).

It is worth noting that not all the above GRs will appear for a specific sample. The crusher is critical to obtain good $^{40}\text{Ar}/^{39}\text{Ar}$ dating results. Different crushing techniques may obtain quite different $^{40}\text{Ar}/^{39}\text{Ar}$ dating results. A defective crusher with a poor fitting between the pestle and the tube's bottom may result in scattered data points and obtain incorrect inverse isochron ages with poor linear correlations (H.N. Qiu, unpub. data, 2008).

$^{40}\text{Ar}/^{39}\text{Ar}$ isochron ages of PFIs in quartz

When excluding nonradiogenic ^{40}Ar using the modern atmospheric $^{40}\text{Ar}/^{36}\text{Ar}$ ratio of 298.56, all nine quartz samples by progressive crushing yield concave (saddle-shaped) or declining age spectra due to excess ^{40}Ar trapped in the quartz.

The inverse isochron plots based on the $^{36}\text{Ar}/^{40}\text{Ar}$ versus $^{39}\text{Ar}/^{40}\text{Ar}$ ratios can usually yield true ages in spite of the presence of excess ^{40}Ar . According to the characteristics of age spectra and the distribution of data points on the inverse isochron plots, we can distinguish the contributions of secondary and primary fluid inclusions (see discussion above). The PFI data points of the nine quartz samples define isochron lines corresponding to ages of 153.7–149.9 Ma with an average of 151.6 ± 0.6 Ma, which are concordant with the mica plateau ages and cassiterite U-Pb ages, providing further constraint on the W-Sn mineralization ages.

Now we further interpret the $^{40}\text{Ar}/^{39}\text{Ar}$ data of the quartz samples based on their characteristics of age spectra and isochron data points.

Single isochron line of PFIs: In the simple cases of samples 13XT21Q and 79Q, all the data points, except the first three or four steps, define isochron lines corresponding to 153.7 and 151.7 Ma with initial $(^{40}\text{Ar}/^{36}\text{Ar})_0$ ratios of 380.7 and 528.2, which are obviously higher than the modern atmospheric ratio. The isochron ages are interpreted as the contribution of the PFIs containing excess ^{40}Ar because they agree well with the ages of the mica samples from the ores, representing the W-Sn mineralization ages. The data points of the first three or four steps are very close to the Y axis of $^{36}\text{Ar}/^{40}\text{Ar}$, containing excess ^{40}Ar with extremely low potassium and corresponding to abnormally old apparent ages. Therefore, they represent the excess ^{40}Ar trapped within microcracks after crystallization.

On the inverse isochron plots (Fig. 10), the data points from 13XT21Q and 79Q form one isochron line, while the other quartz samples (except 13XT23Q) yield two isochron lines, which will be interpreted as SFIs and PFIs in the next section. It seems that samples 13XT21Q and 79Q contain only PFIs without any SFIs. However, SFIs distributed along microcracks are also found in the thin sections of these samples. These observations likely imply that the SFIs might have formed shortly after crystallization from the same ore-forming fluid of the PFIs, resulting in SFIs that have the same ages and initial $(^{40}\text{Ar}/^{36}\text{Ar})_0$ as the PFIs of samples 13XT21Q and 79Q.

Sample 13XT23Q yields one inverse isochron line for the PFIs with a mineralization age of 149.9 ± 8.5 Ma. This quartz sample was obviously overprinted by a much younger post-mineralization fluid, producing the data points from steps 1–8, which do not define an inverse isochron line for the SFIs.

The excess ^{40}Ar in the PFIs of 13XT21Q and 79Q, with much higher $(^{40}\text{Ar}/^{36}\text{Ar})_0$ ratios of 380.7 and 528.2, respectively, than the modern atmospheric ratio of 298.56, might reveal important information about the ore-forming process: (1) the ore-forming fluid was from the deep crust, (2) the ore-forming environment was a relatively closed system to prevent the escape of the excess ^{40}Ar , and (3) the input of meteoric water was limited; otherwise, the atmospheric argon would mask the excess ^{40}Ar brought with the ore-forming fluid from the deep crust.

Two isochron lines of SFIs and PFIs: In the cases of the other six quartz samples, the data points form two isochron lines for each sample, which are interpreted as the contributions of SFIs and PFIs, respectively, except for the first several steps consisting of trapped excess ^{40}Ar from the microcracks and some intermediate steps of SFIs mixed with PFIs.

All the PFI isochron lines (blue lines and solid circle points) of the six quartz samples yield very concordant ore-forming ages of 152.1–150.2 Ma, corresponding to two cases of initial $(^{40}\text{Ar}/^{36}\text{Ar})_0$ ratios: higher than and equal to the modern atmospheric ratio of 298.56. The case of higher initial $(^{40}\text{Ar}/^{36}\text{Ar})_0$ has been discussed above. The case of modern atmosphere $(^{40}\text{Ar}/^{36}\text{Ar})_0$ initially might suggest two possibilities: (1) the deep excess ^{40}Ar in ore-forming fluid has been released to the surface through faults in an open system or (2) meteoric water has mixed with the ore-forming fluid to mask the excess ^{40}Ar from the deep reservoir. The stable isotopes of H and O (App. 4) suggest a magmatic water origin of the quartz. It is the first time that the PFI data points (blue circles) from 13XT08Q and 34Q (Fig. 10f, i) are below the SFI lines toward the x-axis with very high radiogenic $^{40}\text{Ar}_R$ (76.3–86.4% and 88.4–92.6%, respectively) and initial $(^{40}\text{Ar}/^{36}\text{Ar})_0$ ratios of the modern atmospheric value. Therefore, the first possibility above (deep excess ^{40}Ar) is more reasonable considering the H-O isotope components and very high radiogenic $^{40}\text{Ar}_R$ in the quartz samples.

All the SFI isochron lines (green lines and square points in Fig. 10) correspond to higher initial $(^{40}\text{Ar}/^{36}\text{Ar})_0$ ratios than that of the modern atmosphere, showing the presence of excess ^{40}Ar from deep degassing. The SFI ages indicate three periods of hydrothermal fluid activities: ~142, 127–119, and 88–85 Ma.

Our progressive crushing technique certainly releases gases from both SFIs and PFIs sequentially; however, the gas release sequence is always from microcracks, SFIs, PFIs to solid lattices, and from large to small inclusions (Qiu and Jiang, 2007; Qiu and Wijbrans, 2008; Jiang et al., 2012; Bai et al., 2019; Xiao et al., 2019). We have proposed a gas mixing pattern (Bai et al., 2013) and made further modifications (Bai et al., 2018a), which indicate that the gas mixing lines yield the PFI ages and that an intermediate age between the PFI and SFI ages cannot be obtained, because the progressive crushing technique never releases gas mixtures with a constant PFI/SFI proportion for each step. We can usually interpret the $^{40}\text{Ar}/^{39}\text{Ar}$ crushing data in a simple way as in the case of this study.

Summary about mineralization ages

New geochronological data obtained in this study are summarized in Table 1, and available geochronological data from previous studies on the Xitian deposit are summarized in Appendix 5 and shown in Figure 11.

The high-precision $^{40}\text{Ar}/^{39}\text{Ar}$ plateau ages of mica from quartz veins and greisen ores provide well-constrained mineralization ages of 151.8–148.1 Ma for the Xitian W-Sn deposit. The cassiterite LA-ICP-MS U-Pb ages of 151.7–149.7 Ma and quartz PFI $^{40}\text{Ar}/^{39}\text{Ar}$ isochron ages of 153.7–149.9 Ma are also concordant with the mica $^{40}\text{Ar}/^{39}\text{Ar}$ plateau ages within analytical uncertainty. The quartz $^{40}\text{Ar}/^{39}\text{Ar}$ progressive crushing technique can distinguish the SFIs from the PFIs and define a PFI isochron and sometimes an SFI isochron corresponding to geologically meaningful ages, which can be widely applied to determine the mineralization ages of hydrothermal ore deposits.

Geologic significance of quartz SFI ages

Multiple, large-scale Mesozoic W-Sn polymetallic metallogenic events in the Nanling Range generated one of the most important W-Sn metallogenic belts in the world (Mao et al., 2007; Yuan, 2017). J.W. Mao et al. (2013) summarized the temporal-spatial distribution of the Mesozoic diagenesis and mineralization in South China and divided it into three metallogenic episodes: Late Triassic (230–210 Ma), Mid-Late Jurassic (170–150 Ma), and Early-Mid Cretaceous (120–80 Ma). They proposed a period of weak magmatism and insignificant mineralization at 150–120 Ma in the South China block, while a very important mineralization period occurred at 145–137 Ma in North China, Northeast China, and the Middle-Lower Yangtze River Valley belt (Mao, J.W., et al., 2003, 2011, 2013;

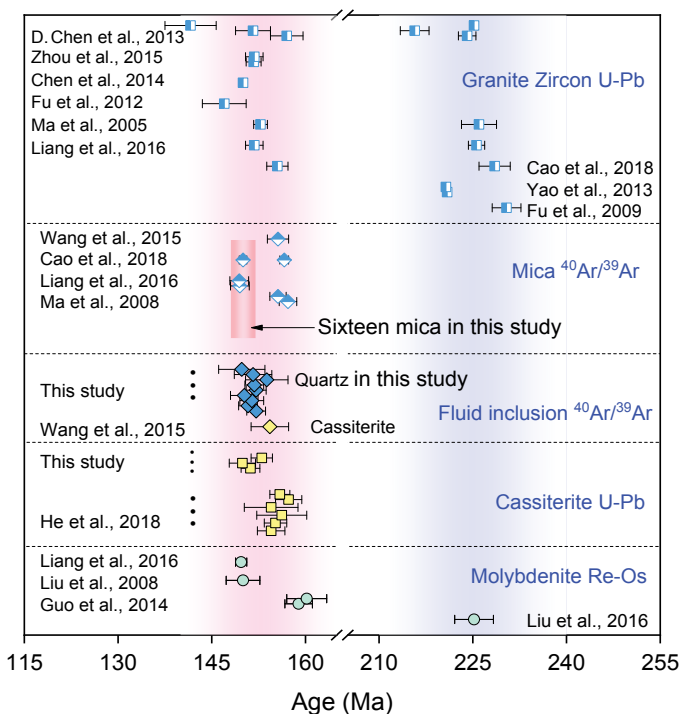


Fig. 11. Compilation of available ages for magmatic and hydrothermal W-Sn mineralization episodes from the Xitian W-Sn polymetallic deposit. (The dates are summarized in App. 5.)

Zhou et al., 2008). A significant W-Sn mineralization epoch has been recently proven to have taken place at 145–130 Ma in the areas adjacent to the Nanling Range (Fig. 12): (1) in North Jiangxi, Dahutang (Mao, Z.H., et al., 2013; Huang and Jiang, 2014) and Zhuxi (Pan et al., 2017) and (2) in the Southeastern Coastal metallogenic belt of tin-bearing porphyry in east Guangdong, Xiling (Liu et al., 2018), Tashan (Yan et al., 2018), Feie'shan (Liu et al., 2017), Jinkeng (Qiu et al., 2017), and Taoxihu (Yan et al., 2017).

Rhenium-osmium geochronology of molybdenite from the Heshuxia mining district of the Xitian W-Sn polymetallic deposit indicated that mineralization slightly younger than the Late Jurassic main W-Sn mineralization occurred at ~142 Ma (Fu et al., 2009). D. Chen et al. (2013) reported a robust zircon U-Pb age from fine-grained granite in the Xitian pluton of 141.6 ± 4.1 Ma (MSWD = 3.9), which proved the occurrence of Early Cretaceous magmatism in the Xitian-Dengfuxian district. The Dengfuxian pluton, about 10 km away north from Xitian, has geochemistry and zircon U-Pb ages of 145–142 Ma

Table 1. Geochronological Data Obtained in This Study

Mineral	Sample number	Method	Age range (Ma)	Mean age (Ma, $\pm 2\sigma$)
Granitic biotite	3	$^{40}\text{Ar}/^{39}\text{Ar}$ plateau age, step heating	152.4–151.6	151.9 ± 0.9
Ore muscovite	11	$^{40}\text{Ar}/^{39}\text{Ar}$ plateau age, step heating	151.8–148.1	149.9 ± 0.6
Greisen biotite	2	$^{40}\text{Ar}/^{39}\text{Ar}$ plateau age, step heating	149.0–148.8	148.9 ± 1.0
Cassiterite	3 samples (96 points)	LA-ICP-MS U-Pb age	151.7–149.7	151.0 ± 1.1
PFIs of quartz	9	$^{40}\text{Ar}/^{39}\text{Ar}$ isochron age, progressive crushing	153.7–149.9	151.6 ± 0.6

LA-ICP-MS = laser ablation-inductively coupled plasma-mass spectrometry, PFIs = primary fluid inclusions

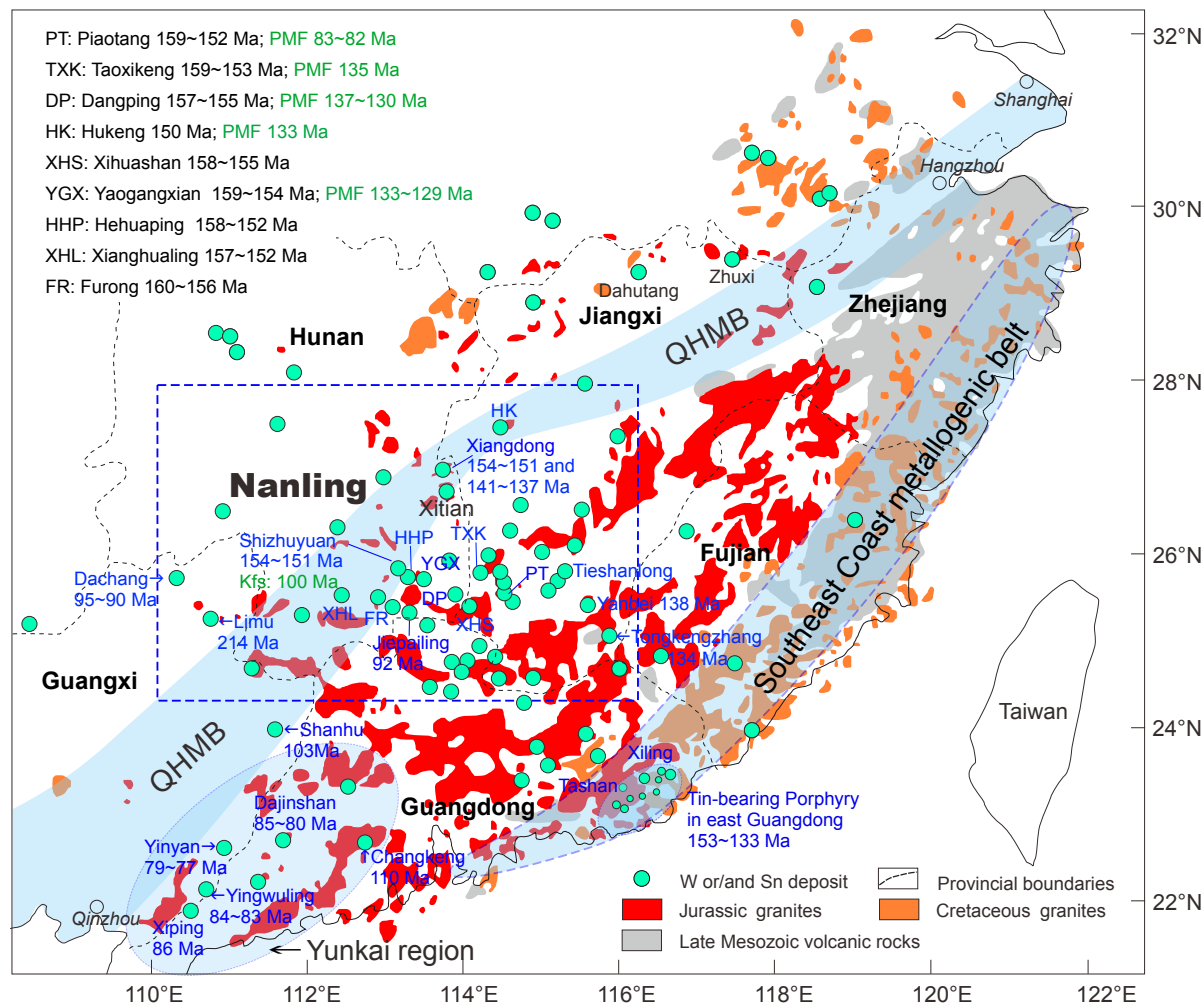


Fig. 12. Geochronology of W-Sn mineralization and postmineralization fluid (PMF) episodes in central South China (modified after Xiong et al., 2020; the dates are summarized in App. 6). QHMB = Qin-Hang metallogenic belt.

similar to those of the Xitian pluton (Song et al., 2018; Xiong et al., 2020). Xiong et al. (2020) suggested that two independent W-Sn mineralization stages occurred at ~152 and 141–137 Ma in Xiangdong. In our present study, the quartz samples, 13XT09Q and 13XT34Q, yield concordant inverse isochron ages of 142.0 Ma and 142.7 Ma, respectively, for their SFIs (Fig. 10h, i), in accordance with the molybdenite Re-Os age of 142.5–141.5 Ma in the Heshuxia mining district (Fu et al., 2009) and the cassiterite U-Pb ages of 141–137 Ma in the Xiangdong deposit (Xiong et al., 2020), which represent the hydrothermal pulses after the Xitian main mineralization at 152–149 Ma.

As one of the most important metallogenic provinces, the Nanling metallogenic region has been a research focus for many years, and a number of reliable geochronological dates have been obtained to closely constrain the W-Sn mineralization (Fig. 12) (App. 6). The main W-Sn mineralization period in the Nanling region took place in the Late Jurassic (160–150 Ma), followed by the Early Cretaceous mineralization (145–130 Ma) (Mao et al., 2004) (e.g., Yanbei, Li et al., 2018; Tongkengzhang, Xu et al., 2007; Xiangdong, Xiong et al., 2020).

The W-Sn mineralization occurring at 100–75 Ma, e.g., Jiepailing (Yuan et al., 2015; Xie et al., 2016) and Dachang (Guo et al., 2018), is associated with the Late Cretaceous magmatism and with mineralization processes that occurred along the continental margin of eastern Asia from South Korea, via southeast-south margins of China, to South Vietnam (see fig. 3 of Cheng et al., 2016). The later Cretaceous hydrothermal processes have also been recorded in K-feldspar veins and SFIs from wolframite and quartz in Piaotang (Bai et al., 2013, 2018a), as well as SFIs from samples 13XT08Q and 52Q from Xitian (Fig. 10f, e).

Conclusions

High-precision mica $^{40}\text{Ar}/^{39}\text{Ar}$ laser step heating, cassiterite LA-ICP-MS U-Pb analysis, and quartz $^{40}\text{Ar}/^{39}\text{Ar}$ progressive crushing are employed to date the mineralization ages of the Longshang and Tongmushan mining districts of the Xitian W-Sn polymetallic deposit. The main conclusions of the present work are summarized as follows:

1. Muscovite and biotite from the ores by laser step heating yield very flat $^{40}\text{Ar}/^{39}\text{Ar}$ age spectra with high-precision

- plateau ages, providing well-constrained mineralization ages of 152.4–148.1 Ma for the Xitian deposit.
2. The cassiterite U-Pb ages (151.6–149.5 Ma) are consistent with the mica $^{40}\text{Ar}/^{39}\text{Ar}$ plateau ages, providing a direct determination technique for ore minerals.
 3. Quartz $^{40}\text{Ar}/^{39}\text{Ar}$ progressive crushing can distinguish the PFIs from the SFIs and yield significant PFI isochron ages (153.7–149.9 Ma), which are in agreement with the mica plateau ages and the cassiterite U-Pb ages. This indicates that the $^{40}\text{Ar}/^{39}\text{Ar}$ progressive crushing technique is a valid approach to obtain hydrothermal mineralization ages and could be widely applied to date geologic events associated with K-bearing fluids.
 4. The $^{40}\text{Ar}/^{39}\text{Ar}$ progressive crushing technique can sometimes yield SFI isochron ages as well, which record the postmineralization hydrothermal activities (~142, 127–119, and 87.9–85.9 Ma) in Xitian.
 5. The initial $(^{40}\text{Ar}/^{36}\text{Ar})_0$ ratio of an inverse isochron line might indicate the environment where the fluid was trapped. Almost all $(^{40}\text{Ar}/^{36}\text{Ar})_0$ of the SFIs are higher than the modern atmospheric value of 298.56, indicating excess ^{40}Ar within the SFIs, which probably reveals that the postmineralization fluids were from deep degassing and were trapped in relatively closed environments. The ore-forming fluids of the granite-associated tin-tungsten deposits were from the deep crust with excess ^{40}Ar . The $(^{40}\text{Ar}/^{36}\text{Ar})_0$ ratios of the PFIs are higher than the modern atmospheric value, possibly indicating relatively closed environments during mineralization, while the $(^{40}\text{Ar}/^{36}\text{Ar})_0$ ratios of the PFIs near the modern atmospheric value imply open environments, which resulted in the escape of the excess ^{40}Ar .

Acknowledgments

We are grateful to Lawrence Meinert, Massimo Chiaradia, Jan Wijbrans, Richard Spikings, and Louise Bolge for their constructive comments, which greatly improved the final manuscript. We would like to thank Rongqing Zhang and Congying Li for helpful discussions, Dan Wu and Wen Zhang for cassiterite U-Pb analyses, and Xuewen Liu for the field work. $^{40}\text{Ar}/^{39}\text{Ar}$ dating samples were irradiated in the newly built China Mianyang Research Reactor (CMRR) under the Earthtime-CN collaboration supported by a Natural Science Foundation of China (NSFC) key project (41630315). This study was also supported by the NSFC projects (41873017, 41688103), the Ministry of Education (MOE) 111 project (B20045), the China University of Geosciences Fundamental Research Funds (CUGQY1913), and the open fund from the MOE Key Laboratory of Tectonics and Petroleum Resources (TPR-2018-20).

REFERENCES

- Andrawes, F., Holzer, G., Roedder, E., Gibson, E.K., Jr., and Oro, J., 1984, Gas chromatographic analysis of volatiles in fluid and gas inclusions: *Journal of Chromatography A*, v. 302, p. 181–193.
- Bai, X.J., Wang, M., Jiang, Y.D., and Qiu, H.N., 2013, Direct dating of tin-tungsten mineralization of the Piaotang tungsten deposit, South China, by $^{40}\text{Ar}/^{39}\text{Ar}$ progressive crushing: *Geochimica et Cosmochimica Acta*, v. 114, p. 1–12.
- Bai, X.J., Jiang, Y.D., Hu, R.G., Gu, X.P., and Qiu, H.N., 2018a, Revealing mineralization and subsequent hydrothermal events: Insights from $^{40}\text{Ar}/^{39}\text{Ar}$ isochron and novel gas mixing lines of hydrothermal quartzes by progressive crushing: *Chemical Geology*, v. 483, p. 332–341.
- Bai, X.J., Qiu, H.N., Liu, W.G., and Mei, L.F., 2018b, Automatic $^{40}\text{Ar}/^{39}\text{Ar}$ dating techniques using multicollector ARGUS VI noble gas mass spectrometer with self-made peripheral apparatus: *Journal of Earth Science*, v. 29, p. 408–415.
- Bai, X.J., Hu, R.G., Jiang, Y.D., Liu, X., Tang, B., and Qiu, H.N., 2019, Refined insight into $^{40}\text{Ar}/^{39}\text{Ar}$ progressive crushing technique from K-Cl-Ar correlations in fluid inclusions: *Chemical Geology*, v. 515, p. 37–49.
- Blamey, N.J.F., 2012, Composition and evolution of crustal, geothermal and hydrothermal fluids interpreted using quantitative fluid inclusion gas analysis: *Journal of Geochemical Exploration*, v. 116–117, p. 17–27.
- Cao, J.Y., Wu, Q.H., Yang, X.Y., Kong, H., Li, H., Xi, X.S., Huang, Q.F., and Liu, B., 2018, Geochronology and genesis of the Xitian W-Sn polymetallic deposit in eastern Hunan Province, South China: Evidence from zircon U-Pb and muscovite Ar-Ar dating, petrochemistry, and wolframite Sr-Nd-Pb isotopes: *Minerals*, v. 8, article 111.
- Carr, P.A., Zink, S., Bennett, V.C., Norman, M.D., Amelin, Y., and Blevin, P.L., 2020, A new method for U-Pb geochronology of cassiterite by ID-TIMS applied to the Mole granite polymetallic system, eastern Australia: *Chemical Geology*, v. 539, article 119539.
- Charvet, J., 2013, The Neoproterozoic-early Paleozoic tectonic evolution of the South China block: An overview: *Journal of Asian Earth Sciences*, v. 74, p. 198–209.
- Chen, D., Ma, A.J., Liu, W., Liu, Y.R., and Ni, Y.J., 2013, Research on U-Pb chronology in Xitian pluton of Hunan Province: *Geoscience*, v. 27, p. 819–830 (in Chinese with English abs.).
- Chen, J., Lu, J.J., Chen, W.F., Wang, R.C., Ma, D.S., Zhu, J.C., Zhang, W.L., and Ji, J.F., 2008, W-Sn-Nb-Ta-bearing granites in the Nanling range and their relationship to metallogenesis: *Geological Journal of China Universities*, v. 14, p. 459–473 (in Chinese with English abs.).
- Chen, J., Wang, R.C., Zhu, J.C., Lu, J.J., and Ma, D.S., 2013, Multiple-aged granitoids and related tungsten-tin mineralization in the Nanling Range, South China: *Science China-Earth Sciences*, v. 56, p. 2045–2055.
- Chen, J.F., and Jahn, B.M., 1998, Crustal evolution of southeastern China: Nd and Sr isotopic evidence: *Tectonophysics*, v. 284, p. 101–133.
- Chen, X.C., Hu, R.Z., Bi, X.W., Li, H.M., Lan, J.B., Zhao, C.H., and Zhu, J.J., 2014, Cassiterite LA-MC-ICP-MS U/Pb and muscovite $^{40}\text{Ar}/^{39}\text{Ar}$ dating of tin deposits in the Tengchong-Lianghe tin district, NW Yunnan, China: *Mineralium Deposita*, v. 49, p. 843–860.
- Cheng, Y.B., Mao, J.W., and Liu, P., 2016, Geodynamic setting of Late Cretaceous Sn-W mineralization in southeastern Yunnan and northeastern Vietnam: *Solid Earth Sciences*, v. 1, p. 79–88.
- Chew, D.M., Sylvester, P.J., and Tubrett, M.N., 2011, U-Pb and Th-Pb dating of apatite by LA-ICPMS: *Chemical Geology*, v. 280, p. 200–216.
- Chew, D.M., Petrus, J.A., and Kamber, B.S., 2014, U-Pb LA-ICPMS dating using accessory mineral standards with variable common Pb: *Chemical Geology*, v. 363, p. 185–199.
- Dalrymple, G.B., and Lanphere, M.A., 1974, $^{40}\text{Ar}/^{39}\text{Ar}$ age spectra of some undisturbed terrestrial samples: *Geochimica et Cosmochimica Acta*, v. 38, p. 715–738.
- Deckart, K., Féraud, G., and Bertrand, H., 1997, Age of Jurassic continental tholeiites of French Guyana, Surinam and Guinea: Implications for the initial opening of the central Atlantic Ocean: *Earth and Planetary Science Letters*, v. 150, p. 205–220.
- Denison, I.A., William, H.F., and Gile, P.L., 1929, Alteration of muscovite and biotite in the soil: U.S. Department of Agriculture, Technical Bulletin 128, p. 1–32.
- Fu, J.M., Wu, S.C., Xu, D.M., Ma, L.Y., Cheng, S.B., and Chen, X.Q., 2009, Reconstraint from zircon SHRIMP U-Pb dating on the age of magma intrusion and mineralization in Xitian tungsten-tin polymetallic orefield, eastern Hunan Province: *Geology and Mineral Resources of South China*, v. 3, p. 1–7 (in Chinese with English abs.).
- Fu, J.M., Cheng, S.B., Lu, Y.Y., Wu, S.C., Ma, L.Y., and Chen, X.Q., 2012, Geochronology of the greisen-quartz-vein type tungsten-tin deposit and its host granite in Xitian, Hunan Province: *Geology and Prospecting*, v. 48, p. 313–320 (in Chinese with English abs.).
- Gao, S., Ling, W.L., Qiu, Y.M., Lian, Z., Hartmann, G., and Simon, K., 1999, Contrasting geochemical and Sm-Nd isotopic compositions of Archean metasediments from the Kongling high-grade terrain of the Yangtze craton: Evidence for cratonic evolution and redistribution of REE during crustal anatexis: *Geochimica et Cosmochimica Acta*, v. 63, p. 2071–2088.

- Graney, J.R., and Kesler, S.E., 1995, Factors affecting gas analysis of inclusion fluid by quadrupole mass spectrometry: *Geochimica et Cosmochimica Acta*, v. 59, p. 3977–3986.
- Gulson, B.L., and Jones, M.T., 1992, Cassiterite: Potential for direct dating of mineral deposits and a precise age for the Bushveld Complex granites: *Geology*, v. 20, p. 355–358.
- Guo, C.L., Li, C., Wu, S.C., and Xu, Y.M., 2014, Molybdenite Re-Os isotopic dating of Xitian deposit in Hunan Province and its geological significance: *Rock and Mineral Analysis*, v. 33, p. 142–152 (in Chinese with English abs.).
- Guo, J., Zhang, R.Q., Sun, W.D., Ling, M.X., Hu, Y.B., Wu, K., Luo, M., and Zhang, L.C., 2018, Genesis of tin-dominant polymetallic deposits in the Dachang district, South China: Insights from cassiterite U-Pb ages and trace element compositions: *Ore Geology Reviews*, v. 95, p. 863–879.
- Harrison, T.M., Celerier, J., Aikman, A.B., Hermann, J., and Heizler, M.T., 2009, Diffusion of ^{40}Ar in muscovite: *Geochimica et Cosmochimica Acta*, v. 73, p. 1039–1051.
- He, M., Hou, Q.L., Liu, Q., Zhang, J.H., Sun, J.F., Wu, S.C., and Zhu, H.F., 2018, Timing and structural controls on skarn-type and vein-type mineralization at the Xitian tin-polymetallic deposit, Hunan Province, SE China: *Acta Geochimica*, v. 37, p. 295–309.
- Hu, R.Z., and Zhou, M.F., 2012, Multiple Mesozoic mineralization events in South China—an introduction to the thematic issue: *Mineralium Deposita*, v. 47, p. 579–588.
- Hua, R.M., Chen, P.R., Zhang, W.L., Liu, X.D., Lu, J.J., Lin, J.F., Yao, J.M., Qi, H.W., Zhang, Z.S., and Gu, S.Y., 2003, Metallogenic systems related to Mesozoic and Cenozoic granitoids in South China: *Science in China Series D: Earth Sciences*, v. 46, p. 816–829.
- Huang, L.C., and Jiang, S.Y., 2014, Highly fractionated S-type granites from the giant Dahutang tungsten deposit in Jiangnan orogen, southeast China: Geochronology, petrogenesis and their relationship with W-mineralization: *Lithos*, v. 202, p. 207–226.
- Jiang, Y.D., Qiu, H.N., and Xu, Y.G., 2012, Hydrothermal fluids, argon isotopes and mineralization ages of the Fankou Pb-Zn deposit in South China: Insights from sphalerite $^{40}\text{Ar}/^{39}\text{Ar}$ progressive crushing: *Geochimica et Cosmochimica Acta*, v. 84, p. 369–379.
- Kelley, S., Turner, G., Butterfield, A.W., and Shepherd, T.J., 1986, The source and significance of argon isotopes in fluid inclusions from areas of mineralization: *Earth and Planetary Science Letters*, v. 79, p. 303–318.
- Kendrick, M.A., Burgess, R., Patrick, R.A.D., and Turner, P.G., 2001, Halogen and Ar-Ar age determinations of inclusions within quartz veins from porphyry copper deposits using complementary noble gas extraction techniques: *Chemical Geology*, v. 177, p. 351–370.
- Kendrick, M.A., Miller, J.M., and Phillips, D., 2006, Part II. Evaluation of $^{40}\text{Ar}/^{39}\text{Ar}$ quartz ages: Implications for fluid inclusion retentivity and determination of initial $^{40}\text{Ar}/^{36}\text{Ar}$ values in Proterozoic samples: *Geochimica et Cosmochimica Acta*, v. 70, p. 2562–2576.
- Lee, J.Y., Marti, K., Severinghaus, J.P., Kawamura, K., Yoo, H.S., Lee, J.B., and Kim, J.S., 2006, A redetermination of the isotopic abundances of atmospheric Ar: *Geochimica et Cosmochimica Acta*, v. 70, p. 4507–4512.
- Li, C.Y., Zhang, R.Q., Ding, X., Ling, M.X., Fan, W.M., and Sun, W.D., 2016, Dating cassiterite using laser ablation ICP-MS: *Ore Geology Reviews*, v. 72, part 1, p. 313–322.
- Li, Q., Zhao, K.D., Lai, P.C., Jiang, S.Y., and Chen, W., 2018, Petrogenesis of Cretaceous volcanic-intrusive complex from the giant Yanbei tin deposit, South China: Implication for multiple magma sources, tin mineralization, and geodynamic setting: *Lithos*, v. 296–299, p. 163–180.
- Li, X.H., Li, Z.X., He, B., Li, W.X., Li, Q.L., Gao, Y.Y., and Wang, X.C., 2012, The early Permian active continental margin and crustal growth of the Cathaysia block: In situ U-Pb, Lu-Hf and O isotope analyses of detrital zircons: *Chemical Geology*, v. 328, p. 195–207.
- Liang, X.Q., Dong, C.G., Jiang, Y., Wu, S.C., Zhou, Y., Zhu, H.F., Fu, J.G., Wang, C., and Shan, Y.H., 2016, Zircon U-Pb, molybdenite Re-Os and muscovite Ar-Ar isotopic dating of the Xitian W-Sn polymetallic deposit, eastern Hunan Province, South China, and its geological significance: *Ore Geology Reviews*, v. 78, p. 85–100.
- Liu, J., Wu, G., Qiu, H.N., and Li, Y., 2015, $^{40}\text{Ar}/^{39}\text{Ar}$ dating, fluid inclusions and S-Pb isotope systematics of the Shabaosi gold deposit, Heilongjiang Province, China: *Geological Journal*, v. 50, p. 592–606.
- Liu, M., Qiu, H.N., Bai, X.J., Xiao, M., and He, L.Y., 2015, Fluid inclusion studies of Xintian tin-tungsten polymetallic deposit in Hunan Province: *Mineral Deposits*, v. 34, p. 981–998 (in Chinese with English abs.).
- Liu, P., Mao, J.W., Cheng, Y.B., Yao, W., Wang, X.Y., and Hao, D., 2017, An Early Cretaceous W-Sn deposit and its implications in southeast coastal metallogenic belt: Constraints from U-Pb, Re-Os, Ar-Ar geochronology at the Feie'shan W-Sn deposit, SE China: *Ore Geology Reviews*, v. 81, p. 112–122.
- Liu, P., Mao, J.W., Santosh, M., Xu, L.G., Zhang, R.Q., and Jia, L.H., 2018, The Xiling Sn deposit, eastern Guangdong province, southeast China: A new genetic model from $^{40}\text{Ar}/^{39}\text{Ar}$ muscovite and U-Pb cassiterite and zircon geochronology: *Economic Geology*, v. 113, p. 511–530.
- Liu, Y., Hu, Z., Gao, S., Guenther, D., Xu, J., Gao, C., and Chen, H., 2008, In situ analysis of major and trace elements of anhydrous minerals by LA-ICP-MS without applying an internal standard: *Chemical Geology*, v. 257, p. 34–43.
- Liu, Y., Gao, S., Hu, Z., Gao, C., Zong, K., and Wang, D., 2010, Continental and oceanic crust recycling-induced melt-peridotite interactions in the Trans-North China orogen: U-Pb dating, Hf isotopes and trace elements in zircons from mantle xenoliths: *Journal of Petrology*, v. 51, p. 537–571.
- Ludwig, K.R., 2008, User's manual for Isoplot/Ex version 3.70: A geochronology toolkit for Microsoft Excel: Berkeley Geochronology Center, Special Publication 4, 76 p.
- Ma, L.Y., Fu, J.M., Wu, S.C., Xu, D.M., and Yang, X.J., 2008, $^{40}\text{Ar}/^{39}\text{Ar}$ isotopic dating of the Longshang tin-polymetallic deposit, Xitian orefield, eastern Hunan: *Geology of China*, v. 35, p. 706–713.
- Ma, T.Q., Bai, D.Y., Kuang, J., and Wang, X.H., 2005, Zircon SHRIMP dating of the Xitian granite pluton, Chaling, southeastern Hunan, and its geological significance: *Geological Bulletin of China*, v. 24, p. 415–419 (in Chinese with English abs.).
- Mao, J.W., Wang, Y.T., Zhang, Z.H., Yu, J.J., and Niu, B.G., 2003, Geodynamic settings of Mesozoic large-scale mineralization in North China and adjacent areas—implication from the highly precise and accurate ages of metal deposits: *Science in China Series D—Earth Sciences*, v. 46, p. 838–851.
- Mao, J.W., Xie, G.Q., Li, X.F., Zhang, C.Q., and Mei, Y.X., 2004, Mesozoic large scale mineralization and multiple lithospheric extension in South China: *Earth Science Frontiers*, v. 11, p. 45–55 (in Chinese with English abs.).
- Mao, J.W., Xie, G.Q., Guo, C.L., and Chen, Y.C., 2007, Large-scale tungsten-tin mineralization in the Nanling region, South China: Metallogenic ages and corresponding geodynamic processes: *Acta Petrologica Sinica*, v. 23, p. 2329–2338 (in Chinese with English abs.).
- Mao, J.W., Xie, G.Q., Duan, C., Pirajno, F., Ishiyama, D., and Chen, Y.C., 2011, A tectono-genetic model for porphyry-skarn-stratabound Cu-Au-Mo-Fe and magnetite-apatite deposits along the Middle-Lower Yangtze River Valley, eastern China: *Ore Geology Reviews*, v. 43, p. 294–314.
- Mao, J.W., Cheng, Y., Chen, M., and Franco, P., 2013, Major types and time-space distribution of Mesozoic ore deposits in South China and their geodynamic settings: *Mineralium Deposita*, v. 48, p. 267–294.
- Mao, Z.H., Cheng, Y.B., Liu, J.J., Yuan, S.D., Wu, S.H., Xiang, X.K., and Luo, X.H., 2013, Geology and molybdenite Re-Os age of the Dahutang granite-related veinlets-disseminated tungsten ore field in the Jiangxin Province, China: *Ore Geology Reviews*, v. 53, p. 422–433.
- Mark, D.F., Barfod, D., Stuart, F.M., and Imlach, J., 2009, The ARGUS multicollector noble gas mass spectrometer: Performance for $^{40}\text{Ar}/^{39}\text{Ar}$ geochronology: *Geochemistry Geophysics Geosystems*, v. 10, article Q0AA02.
- McDougall, I., and Harrison, T.M., 1999, *Geochronology and thermochronology by the $^{40}\text{Ar}/^{39}\text{Ar}$ method (2nd ed.)*: New York, Oxford University Press, 269 p.
- Moscati, R.J., and Neymark, L.A., 2020, U-Pb geochronology of tin deposits associated with the Cornubian batholith of southwest England: Direct dating of cassiterite by in situ LA-ICPMS: *Mineralium Deposita*, v. 55, p. 1–20.
- Pan, X.F., Hou, Z.Q., Li, Y., Chen, G.H., Zhao, M., Zhang, T.F., Zhang, C., Wei, J., and Kang, C., 2017, Dating the giant Zhuxi W-Cu deposit (Taquan-Fuchun Ore belt) in South China using molybdenite Re-Os and muscovite Ar-Ar system: *Ore Geology Reviews*, v. 86, p. 719–733.
- Pfänder, J.A., Sperner, B., Ratschbacher, L., Fischer, A., Meyer, M., Leistner, M., and Schaeben, H., 2014, High-resolution $^{40}\text{Ar}/^{39}\text{Ar}$ dating using a mechanical sample transfer system combined with a high-temperature cell for step heating experiments and a multicollector ARGUS noble gas mass spectrometer: *Geochemistry Geophysics Geosystems*, v. 15, p. 2713–2726.
- Qiu, H.N., 1996, $^{40}\text{Ar}/^{39}\text{Ar}$ dating of the quartz samples from two mineral deposits in western Yunnan (SW China) by crushing in vacuum: *Chemical Geology*, v. 127, p. 211–222.
- Qiu, H.N., and Dai, T.M., 1989, $^{40}\text{Ar}/^{39}\text{Ar}$ techniques for dating the fluid inclusions of quartz from a hydrothermal deposit: *Chinese Science Bulletin*, v. 34, p. 1887–1890.

- Qiu, H.N., and Jiang, Y.D., 2007, Sphalerite $^{40}\text{Ar}/^{39}\text{Ar}$ progressive crushing and stepwise heating techniques: *Earth and Planetary Science Letters*, v. 256, p. 224–232.
- Qiu, H.N., and Wijbrans, J.R., 2006, Paleozoic ages and excess ^{40}Ar in garnets from the Bixiling eclogite in Dabieshan, China: New insights from $^{40}\text{Ar}/^{39}\text{Ar}$ dating by stepwise crushing: *Geochimica et Cosmochimica Acta*, v. 70, p. 2354–2370.
- , 2008, The Paleozoic metamorphic history of the Central orogenic belt of China from $^{40}\text{Ar}/^{39}\text{Ar}$ geochronology of eclogite garnet fluid inclusions: *Earth and Planetary Science Letters*, v. 268, p. 501–514.
- Qiu, H.N., Wu, H.Y., Yun, J.B., Feng, Z.H., Xu, Y.G., Mei, L.F., and Wijbrans, J.R., 2011, High-precision $^{40}\text{Ar}/^{39}\text{Ar}$ age of the gas emplacement into the Songliao basin: *Geology*, v. 39, p. 451–454.
- Qiu, Y., and Gao, S., 2000, First evidence of >3.2 Ga continental crust in the Yangtze craton of South China and its implications for Archean crustal evolution and Phanerozoic tectonics: *Geology*, v. 28, p. 11–14.
- Qiu, Z.W., Yan, Q.H., Li, S.S., Wang, H., Tong, L., Zhang, R.Q., Wei, X.P., Li, P., Wang, L.M., Bu, A., and Yan, L.M., 2017, Highly fractionated Early Cretaceous I-type granites and related Sn polymetallic mineralization in the Jinkeng deposit, eastern Guangdong, SE China: Constraints from geochronology, geochemistry, and Hf isotopes: *Ore Geology Reviews*, v. 88, p. 718–738.
- Schaen, A.J., Jicha, B.R., Hodges, K.V., Vermeesch, P., Stelten, M.E., Mercer, C.M., Phillips, D., Rivera, T.A., Jourdan, F., Matchan, E.L., et al., 2021, Interpreting and reporting $^{40}\text{Ar}/^{39}\text{Ar}$ geochronologic data: *Geological Society of America Bulletin*, v. 133, p. 461–487.
- Simonetti, A., Heaman, L.M., Chacko, T., and Banerjee, N.R., 2006, In situ petrographic thin section U-Pb dating of zircon, monazite, and titanite using laser ablation-MC-ICP-MS: *International Journal of Mass Spectrometry*, v. 253, p. 87–97.
- Slack, J.F., Neymark, L.A., Moscati, R.J., Lowers, H.A., Ransom, P.W., Hauser, R.L., and Adams, D.T., 2020, Origin of tin mineralization in the Sullivan Pb-Zn-Ag deposit, British Columbia: Constraints from textures, geochemistry, and LA-ICP-MS U-Pb geochronology of cassiterite: *Economic Geology*, v. 115, p. 1699–1724.
- Song, C.J., Ye, Y.Y., and Guo, L., 2018, The study of connected relationship and three-dimensional morphology of Xitian-Dengfuxian plutons in Hunan: *China Science and Technology Achievements*, v. 6, p. 32–36 (in Chinese).
- Tartese, R., Poujol, M., Ruffet, G., Boulvais, P., Yamato, P., and Kosler, J., 2011, New U-Pb zircon and $^{40}\text{Ar}/^{39}\text{Ar}$ muscovite age constraints on the emplacement of the Lizio syn-tectonic granite (Armorican Massif, France): *Comptes Rendus Geoscience*, v. 343, p. 443–453.
- Turner, G., 1988, Hydrothermal fluids and argon isotopes in quartz veins and cherts: *Geochimica et Cosmochimica Acta*, v. 52, p. 1443–1448.
- Turner, G., and Bannon, M.P., 1992, Argon isotope geochemistry of inclusion fluids from granite-associated mineral veins in southwest and northeast England: *Geochimica et Cosmochimica Acta*, v. 56, p. 227–243.
- U.S. Geological Survey (USGS), 2019, Mineral commodity summaries: <http://minerals.usgs.gov/minerals/pubs/mcs/2019/mcs2019.pdf>.
- Villa, I.M., 2001, Radiogenic isotopes in fluid inclusions: *Lithos*, v. 55, p. 115–124.
- Wang, M., Bai, X.J., Hu, R.G., Cheng, S.B., Pu, Z.P., and Qiu, H.N., 2015a, Direct dating of cassiterite in Xitian tungsten-tin polymetallic deposit, south-east Hunan, by $^{40}\text{Ar}/^{39}\text{Ar}$ progressive crushing: *Geotectonica et Metallogenesis*, v. 39, p. 1049–1060 (in Chinese with English abs.).
- Wang, M., Bai, X.J., Yun, J.B., Zhao, L.H., Li, Y.L., Wang, Z.Y., Pu, Z.P., and Qiu, H.N., 2016, $^{40}\text{Ar}/^{39}\text{Ar}$ dating of mineralization of Shizhuyuan polymetallic deposit: *Geochimica*, v. 45, p. 41–51 (in Chinese with English abs.).
- Wang, S.S., 1983, Age determinations of $^{40}\text{Ar}/^{40}\text{K}$, $^{40}\text{Ar}/^{39}\text{Ar}$ and radiogenic ^{40}Ar released characteristics on K-Ar geostandards of China: *Scientia Geologica Sinica*, p. 315–323 (in Chinese with English abs.).
- Wang, Y.J., Fan, W.M., Guo, F., Peng, T.P., and Li, C.W., 2003, Geochemistry of Mesozoic mafic rocks adjacent to the Chenzhou-Linwu fault, South China: Implications for the lithospheric boundary between the Yangtze and Cathaysia blocks: *International Geology Review*, v. 45, p. 263–286.
- Warren, C.J., Hanke, F., and Kelley, S.P., 2012a, When can muscovite $^{40}\text{Ar}/^{39}\text{Ar}$ dating constrain the timing of metamorphic exhumation?: *Chemical Geology*, v. 291, p. 79–86.
- Warren, C.J., Kelley, S.P., Sherlock, S.C., and McDonald, C.S., 2012b, Metamorphic rocks seek meaningful cooling rate: Interpreting $^{40}\text{Ar}/^{39}\text{Ar}$ ages in an exhumed ultra-high pressure terrane: *Lithos*, v. 155, p. 30–48.
- Wheeler, J., 1996, DIFFARG: A program for simulating argon diffusion profiles in minerals: *Computers and Geosciences*, v. 22, p. 919–929.
- Whitney, D.L., and Evans, B.W., 2010, Abbreviations for names of rock-forming minerals: *American Mineralogist*, v. 95, p. 185–187.
- Wilkinson, J.J., 2001, Fluid inclusions in hydrothermal ore deposits: *Lithos*, v. 55, p. 229–272.
- Xiao, M., Qiu, H.N., Jiang, Y.D., Cai, Y., Bai, X.J., Zhang, W.F., Liu, M., and Qin, C.J., 2019, Gas release systematics of mineral-hosted fluid inclusions during stepwise crushing: Implications for $^{40}\text{Ar}/^{39}\text{Ar}$ geochronology of hydrothermal fluids: *Geochimica et Cosmochimica Acta*, v. 251, p. 36–55.
- Xie, L., Wang, R.C., Che, X.D., Huang, F.F., Erdmann, S., and Zhang, W.L., 2016, Tracking magmatic and hydrothermal Nb-Ta-W-Sn fractionation using mineral textures and composition: A case study from the late Cretaceous Jiepailing ore district in the Nanling Range in South China: *Ore Geology Reviews*, v. 78, p. 300–321.
- Xiong, Y.Q., Shao, Y.J., Cheng, Y.B., and Jiang, S.Y., 2020, Discrete Jurassic and Cretaceous mineralization events at the Xiangdong W(-Sn) deposit, Nanling Range, South China: *Economic Geology*, v. 115, p. 385–413.
- Xu, J.X., Zeng, Z.L., Li, X.Q., Liu, J.S., Chen, Z.H., Liu, S.B., Guo, C.L., and Wang, C.H., 2007, Geological characteristics and mineralization age of the Tongkengzhang molybdenum deposit in Xunwu county, South Jiangxi Province, China: *Acta Geologica Sinica*, v. 81, p. 924–928 (in Chinese with English abs.).
- Yan, Q.H., Li, S.S., Qiu, Z.W., Wang, H., Wei, X.P., Pei, L., Dong, R., and Zhang, X.Y., 2017, Geochronology, geochemistry and Sr-Nd-Hf-S-Pb isotopes of the Early Cretaceous Taoxihu Sn deposit and related granitoids, SE China: *Ore Geology Reviews*, v. 89, p. 350–368.
- Yan, Q.H., Wang, H., Qiu, Z.W., Wang, M., Mu, S.L., Wang, L.M., Bu, A., Wang, S.M., Li, S.S., Wei, X.P., and Li, P., 2018, Zircon and cassiterite U-Pb ages and Lu-Hf isotopic compositions of Tashan tin-bearing porphyry in Guangdong Province, SE China and its geological significance: *Geotectonica et Metallogenesis*, v. 42, p. 718–731 (in Chinese with English abs.).
- Yang, J.H., Zhou, M.F., Hu, R.Z., Zhong, H., Williams Jones, A.E., Liu, L., Zhang, X.C., Fu, Y.Z., and Mao, W., 2020, Granite-related tin metallogenetic events and key controlling factors in Peninsular Malaysia, southeast Asia: New insights from cassiterite U-Pb dating and zircon geochemistry: *Economic Geology*, v. 115, p. 581–601.
- Yao, Y., Chen, J., Lu, J.J., and Zhang, R.Q., 2013, Geochronology, Hf isotopic compositions and geochemical characteristics of Xitian A-type granite and its geological significance: *Mineral Deposits*, v. 32, p. 467–488 (in Chinese with English abs.).
- Yu, J.H., Wang, L.J., O'Reilly, S.Y., Griffin, W.L., Zhang, M., Li, C.Z., and Shu, L.S., 2009, A Paleoproterozoic orogeny recorded in a long-lived cratonic remnant (Wuyishan terrane), eastern Cathaysia block, China: *Precambrian Research*, v. 174, p. 347–363.
- Yuan, S.D., 2017, Several crucial scientific issues related to the W-Sn metallogenesis in the Nanling Range and their implications for regional exploration: A review: *Bulletin of Mineralogy Petrology and Geochemistry*, v. 36, p. 736–749 (in Chinese with English abs.).
- Yuan, S.D., Peng, J.T., Hu, R.Z., Li, H.M., Shen, N.P., and Zhang, D.L., 2008, A precise U-Pb age on cassiterite from the Xianghualing tin-polymetallic deposit (Hunan, South China): *Mineralium Deposita*, v. 43, p. 375–382.
- Yuan, S.D., Peng, J.T., Hao, S., Li, H.M., Geng, J.Z., and Zhang, D.L., 2011, In situ LA-MC-ICP-MS and ID-TIMS U-Pb geochronology of cassiterite in the giant Furong tin deposit, Hunan Province, South China: New constraints on the timing of tin-polymetallic mineralization: *Ore Geology Reviews*, v. 43, p. 235–242.
- Yuan, S.D., Mao, J.W., Cook, N.J., Wang, X.D., Liu, X.F., and Yuan, Y.B., 2015, A Late Cretaceous tin metallogenetic event in Nanling W-Sn metallogenetic province: Constraints from U-Pb, Ar-Ar geochronology at the Jiepailing Sn-Be-F deposit, Hunan, China: *Ore Geology Reviews*, v. 65, p. 283–293.
- Zaw, K., Peters, S.G., Cromie, P., Burrett, C., and Hou, Z., 2007, Nature, diversity of deposit types and metallogenetic relations of South China: *Ore Geology Reviews*, v. 31, p. 3–47.
- Zhang, D.L., Peng, J.T., Coulson, I.M., Hou, L.H., and Li, S.J., 2014, Cassiterite U-Pb and muscovite $^{40}\text{Ar}/^{39}\text{Ar}$ age constraints on the timing of mineralization in the Xuebaoding Sn-W-Be deposit, western China: *Ore Geology Reviews*, v. 62, p. 315–322.
- Zhang, R.Q., Lu, J.J., Wang, R.C., Yang, P., Zhu, J.C., Yao, Y., Gao, J.F., Li, C., Lei, Z.H., Zhang, W.L., and Guo, W.M., 2015, Constraints of in situ zircon and cassiterite U-Pb, molybdenite Re-Os and muscovite $^{40}\text{Ar}/^{39}\text{Ar}$ ages on multiple generations of granitic magmatism and related W-Sn mineralization in the Wangxianling area, Nanling Range, South China: *Ore Geology Reviews*, v. 65, p. 1021–1042.

- Zhang, R.Q., Lu, J.J., Lehmann, B., Li, C.Y., Li, G.L., Zhang, L.P., Guo, J., and Sun, W.D., 2017, Combined zircon and cassiterite U-Pb dating of the Piaotang granite-related tungsten-tin deposit, southern Jiangxi tungsten district, China: *Ore Geology Reviews*, v. 82, p. 268–284.
- Zhao, Z.F., Gao, P., and Zheng, Y.F., 2015, The source of Mesozoic granitoids in South China: Integrated geochemical constraints from the Taoshan batholith in the Nanling Range: *Chemical Geology*, v. 395, p. 11–26.
- Zheng, Y.F., Xiao, W.J., and Zhao, G.C., 2013, Introduction to tectonics of China: *Gondwana Research*, v. 23, p. 1189–1206.
- Zhou, T.F., Fan, Y., and Yuan, F., 2008, Advances on petrogenesis and metallogeny study of the mineralization belt of the Middle and Lower reaches of the Yangtze River area: *Acta Petrologica Sinica*, v. 24, p. 1665–1678.
- Zhou, X.M., Sun, T., Shen, W.Z., Shu, L.S., and Niu, Y.L., 2006, Petrogenesis of Mesozoic granitoids and volcanic rocks in South China: A response to tectonic evolution: *Episodes*, v. 29, p. 26–33.
- Zhou, Y., Liang, X.Q., Wu, S.C., Cai, Y.F., Liang, X.R., Shao, T.B., Wang, C., Fu, J.G., and Jiang, Y., 2015, Isotopic geochemistry, zircon U-Pb ages and Hf isotopes of A-type granites from the Xitian W-Sn deposit, SE China: Constraints on petrogenesis and tectonic significance: *Journal of Asian Earth Sciences*, v. 105, p. 122–139.

Xiujuan Bai is an associate research professor of geochronology at the China University of Geosciences, Wuhan. She received her B.Sc., M.Sc., and Ph.D. degrees in geochemistry at the China University of Geosciences, Wuhan, in 2008, 2011, and 2014, respectively. Her research interests focus on $^{40}\text{Ar}/^{39}\text{Ar}$ dating techniques and their applications in various fields of earth sciences.

